International Journal of Biological Macromolecules 210 (2022) 530–544

Contents lists available at ScienceDirect

International Journal of Biological Macromolecules

journal homepage: www.elsevier.com/locate/ijbiomac

Carboxymethylcellulose biofunctionalized ternary quantum dots for subcellular-targeted brain cancer nanotheranostics

Alexandra A.P. Mansur [a], Mayara R.B. Paiva [b], Oliver A.L. Cotta [b], Luciana M. Silva [b], Isadora C. Carvalho [a], Nádia S.V. Capanema [a], Sandhra M. Carvalho [a], Érica A. Costa [c], Nelson R. Martin [c], Roselene Ecco [c], Beatriz S. Santos [c], Silvia L. Fialho [b,*], Zélia I.P. Lobato [c], Herman S. Mansur [a,*]

[a] Center of Nanoscience, Nanotechnology, and Innovation-CeNano²I, Federal University of Minas Gerais/UFMG, Belo Horizonte, MG, Brazil
[b] Pharmaceutical Research and Development, Ezequiel Dias Foundation, Belo Horizonte, MG, Brazil
[c] Veterinary School, Universidade Federal de Minas Gerais-UFMG, Brazil

ARTICLE INFO

Keywords:
Carboxymethylcellulose nanomedicine
Carboxymethylcellulose-peptide nanohybrids
Polysaccharide-based nanoarchitectures
Cancer nanotheranostics

ABSTRACT

Among the most lethal forms of cancer, malignant brain tumors persist as one of the greatest challenges faced by oncologists, where nanotechnology-driven theranostics can play a critical role in developing novel polymer-based supramolecular nanoarchitectures with multifunctional and multi-modal characteristics to fight cancer. However, it is virtually a consensus that, besides the complexity of active delivering anticancer drugs by the nanocarriers to the tumor site, the current evaluation methods primarily relying on *in vitro* assays and *in vivo* animal models have been accounted for the low translational effectiveness to clinical applications. In this view, the chick chorioallantoic membrane (CAM) assay has been increasingly recognized as one of the best preclinical models to study the effects of anticancer drugs on the tumor microenvironment (TME). Thus, in this study, we designed, characterized, and developed novel hybrid nanostructures encompassing chemically functionalized carboxymethylcellulose (CMC) with mitochondria-targeting pro-apoptotic peptide (KLA) and cell-penetrating moiety (cysteine, CYS) with fluorescent inorganic semiconductor (Ag-In-S, AIS) for simultaneously bioimaging and inducing glioblastoma cancer cell (U-87 MG, GBM) death. The results demonstrated that the CMC-peptide macromolecules produced supramolecular vesicle-like nanostructures with aqueous colloidal stability suitable as nanocarriers for passive and active targeting of cancer tumors. The optical properties and physicochemical features of the nanoconjugates confirmed their suitability as photoluminescent nanoprobes for cell bioimaging and intracellular tracking. Moreover, the results *in vitro* demonstrated a notable killing activity towards GBM cells of cysteine-bearing CMC conjugates coupled with pro-apoptotic KLA peptides. More importantly, compared to doxorubicin (DOX), a model anticancer drug in chemotherapy that is highly toxic, these innovative nano-hybrids nanoconjugates displayed higher lethality against U-87 MG cancer cells. *In vivo* CAM assays validated these findings where the nanohybrids demonstrated a significant reduction of GBM tumor progression (41% area) and evidenced an antiangiogenic activity. These results pave the way for developing polymer-based hybrid nanoarchitectonics applied as targeted multifunctional theranostics for simultaneous imaging and therapy against glioblastoma while possibly reducing the systemic toxicity and side-effects of conventional anticancer chemotherapeutic agents.

1. Introduction

Despite unquestionable progress in recent decades, cancer remains one of the most common causes of death in developed countries. Above all, malignant brain tumors such as glioblastoma (referred to as GBM) are considered one of the most significant challenges because, unfortunately, most patients have an adverse prognosis and high lethality rates [1–6]. In recent years, the amalgamation of nanotechnology with

* Corresponding authors at: Federal University of Minas Gerais, Av. Antônio Carlos, 6627– Escola de Engenharia, Bloco 2 – Sala 2233, 31.270-901 Belo Horizonte, MG, Brazil.
E-mail addresses: silvia.fialho@funed.mg.gov.br (S.L. Fialho), hmansur@demet.ufmg.br (H.S. Mansur).

https://doi.org/10.1016/j.ijbiomac.2022.04.207
Received 5 February 2022; Received in revised form 21 April 2022; Accepted 27 April 2022
Available online 2 May 2022

medicine (termed *nanomedicine*) has emerged as an up-and-coming field of research for offering innovative alternatives to conventional therapies (*e.g.,* chemotherapy, radiotherapy) to treat cancer patients. Conventional chemotherapy usually relies on toxic drugs systemically administered to cancer patients leading to numerous side effects, with narrow therapeutic indexes, and causing multidrug-resistance of brain tumors, including GBM rates [1–6]. Fortunately, cancer nanomedicine has been enabling new multi-modal therapy strategies, including using hybrid nanostructures to develop targeted and optimized drug delivery systems (DDS). They are rationally designed and built, merging multiple components in an integrated nanostructure, often combining bioimaging, targeting, and drug therapy for cancer tumors, while minimizing the side effects [3–11].

The hybrid nanostructures (*nanohybrids*) are usually constructed based on two or more components of distinct nature, including inorganic nanomaterials and organic molecules, rendering a unique set of features and properties impossible to be attainable with each one separately. Essentially, bearing in mind oncology nanomedicine, the inorganic portion of the nanohybrids is made by nanomaterials that can be activated through external stimuli (*e.g.,* optical, magnetic), such as semiconductor quantum dots (*e.g.,* fluorescent quantum dots), metallic nanoparticles (*e.g.,* plasmonic nanometals), metal oxides (*e.g.,* magnetic ferrites, MFe_2O_4) [11–16]. The organic part of nanohybrids, often applied as the shell layer, usually comprises bio-chemically stimuli-responsive components (*e.g.,* pH, ionic strength), such as polymers and biomolecules. They play a pivotal role in the chemical stability as well as in the interactions and activity with the complex biological environment, which can be associated or not with anticancer drugs. More importantly, they also ascribe the biological functionalization for affinity recognition for targeting the cancerous cells at the diseased tumor tissues and organs [8,10,13,16,17].

In this context, as optically active nanomaterials, quantum dots (QDs) are one of the most often applied inorganic nanoparticles for bioimaging, biosensing, and cellular tracking. Over the past few years, compared to fluorescent dyes, QDs have increasingly gained more attention from researchers due to their advantages such as photostability, broad excitation spectra, sharp emission spectra, and significant Stocks shifts, which can also be biofunctionalized with affinity molecules in nanomedicine [17–22]. Besides their physicochemical and optical properties, QDs should also present biocompatibility and meet a more sustainable approach considering a *green* nanomedicine strategy. They have been associated with organic (bio)macromolecules through polymer-based aqueous colloidal processes under *greener* conditions, which is favorable for developing innovative nanohybrids for biomedical and environmentally benign applications [12,20,21,23,24].

On the other end, considering several possibilities of organic components for building nanohybrids, polymer-based nano-assemblies have been preferred as they can produce supramolecular structures that possess the ability to undergo dynamic/reversible changes of conformation, shape, charge distribution, and with excellent functions in response to (bio)chemical stimuli (*i.e.,* pH, concentration, ionic strength, charge potential) making them promising candidates for applications in cancer nanomedicine [10,11,16,25,26]. In this view, polysaccharides (*e.g.,* hyaluronic acid, cellulose, chitosan, and derivatives) have been the most common choice of nature-sourced biocompatible polymers for biomedical and pharmaceutical applications [27]. Specifically, carboxymethylcellulose (CMC), a widely commercially available cellulose derivative, finds wide-ranging applications in biology, biomedicine, and pharmaceutical formulations, including developing nanocarriers for the *smart* delivery of anticancer therapeutic agents [10,12,28,29]. Moreover, it presents exceptional biodegradability, non-toxicity, suitable reactivity for simple chemical modification associated with global availability, and low cost. Besides, CMC polymers possess intrinsic amphiphilic behavior associated with reactive chemical groups (*e.g.,* hydroxyls and carboxyls), which permit their flexible functionalization with biomolecules and interactions with low water-soluble (or insoluble) hydrophobic drugs [28,29] allowing bioconjugates with tailored vesicle-like structures. Importantly, CMC has also been approved by the United States Food and Drug Administration (FDA) in the applications of biotechnology and biomedicine [10,12].

In this sense, polysaccharide-based nanocarriers can be functionalized with affinity biomolecules (*e.g.,* amino acids, peptides, proteins, antibodies) for developing targeted nanoconjugates for reaching cancer tumor sites [1,10,13,15,30]. Especially, peptides are promising affinity biomolecules for designing and developing the next generation of *smart* anticancer therapeutic conjugates compared to protein or antibodies. They possess advantages such as facile synthesis and chemical functionalization combined with lower immunogenicity [1,31]. Yet, as reported in a recent elegant review by Gao et al. [17], the targeted delivery of specific chemotherapeutic agents to the cancer cell and its subcellular organelles is one of the critical difficulties that persist in being answered [32–34]. Thus, the mitochondrion, generally known as the "cell machinery", is a subcellular organelle that can activate apoptosis upon intrinsic or extrinsic stimuli through triggering cell death signaling cascades. Since mitochondrial activities are typically altered in neoplastic cells, targeting this organelle allows inducing different cell death signaling mechanisms and pathways [1,32,33]. In this view, the KLA peptide, an amphiphilic α-helical pro-apoptotic cationic peptide sequence, can interact with the highly negatively charged mitochondrial membrane and cause its disruption, which can be used for constructing active anticancer targeting drugs [32–35]. Due to the inability to enter eukaryotic cells, KLA-bearing nanocarriers depend on a membrane-permeable vehicle, termed cell-penetrating peptides (CPPs, *e.g.,* arginine-rich and cysteine-rich sequences), for efficient intracellular delivery of the chemotherapeutic component [1,34].

Although the research in nano-oncology has remarkably advanced at a rapid pace in recent years, relatively minimal clinical translation of nanotechnology to human applications has been accomplished [9,30,36]. Currently, it is documented that, after the administration of the nanocarrier to the patient, it interacts with the complex biological system along its journey until reaching the actual target tumor location, which forms several barriers that control the delivery process. As a result, it causes harmful systemic side effects and decreases the overall efficacy of the nanoformulations for treating cancer (estimated median of ~0.7% of the injected dose) [37,38]. Specifically, the difficulty of treating GBM with emerging nanomedicines has proven to be drastically more challenging, mainly due to these cancers' unique biological characteristics, which often conspire to hamper the delivery process. GBM tumors are not only often inaccessible for treatment using conventional neurosurgery, but also, they are located behind the blood-brain barrier (BBB), often hindering exposure to conventional systemic chemotherapy [39–41].

Although many studies have shown the potential utility of nanoparticles for detecting, imaging, and killing cancer cells *in vitro* and *in vivo*, their resultant clinical translation has been discouraging [40,42]. That may be credited to several aspects, but they often involve *in vitro* systems or animal models, which are scarcely standardized or inaccurately performed and, therefore, not directly comparable to other related studies [43]. Currently, the mouse model is the most common animal model used for screening potential drugs, even though they are expensive and time-consuming. Furthermore, more strict regulations have been established towards using animal models for research purposes, following the "*3Rs*" concept (*i.e.,* reduction, refinement, and replacement). Hence, there is an urgent demand for additional models for mimicking the tumor microenvironment (TME) [43,44]. In this view, the *in vivo* chick chorioallantoic membrane (CAM) assay (also termed "*in ovo*") has been considered one of the best preclinical models to study the effects of anticancer drugs on the tumor microenvironment TME. It provides researchers with a readily available, accessible, self-sustaining, high throughput screening *in vivo* model without requiring sophisticated animal facilities or approval from animal research ethics committees according to many country regulations [45]. Moreover, the CAM

embryo model is a naturally immune-deficient host, enabling the grafting of tissues of several types of malignant tumors. Also, the blood vessel network of the CAM provides an excellent environment for primary tumor formation and a basis for angiogenic blood vessel formation [46]. The insertion of malignant cells and tumor tissues into the CAM model creates a capable system for investigating cancer growth and the efficiency of several anticancer targeted-therapy responses [44].

Hence, to the best of our knowledge, this is the first study to report the *in vivo* assays using the CAM embryo model supporting the *in vitro* assays with GBM cells, which demonstrated the effective mitochondria-targeted anticancer nanotheranostic activities of novel hybrid inorganic-organic nanoarchitectures composed of ternary quantum dots (AIS) and CMC-Cysteine-KLA biopolymer-peptide macromolecules.

2. Materials and methods

2.1. Materials

Carboxymethylcellulose sodium salt (CMC; degree of substitution, DS = 0.7; molecular weight, M_w = 250 kDa; viscosity = 735 cps, at 25 °C, at 2% in H_2O), 1-Ethyl-3-[3-dimethylaminopropyl]carbodiimide hydrochloride (EDC), N-hydroxysulfosuccinimide sodium salt (sulfo-NHS), L-cysteine hydrochloride (CYS), ethanolamine hydrochloride (ETA), and doxorubicin hydrochloride (DOX) were purchased from Sigma-Aldrich (USA). KLA peptide (sequence LAKLAKKLAKLAK) was designed and purchased from GenScript (USA). All of the other materials, reagents, and precursors used in this study were described in the experimental sections.

2.2. Synthesis of biofunctionalized hybrid nanoconjugates

Ag-In-S ternary quantum dots stabilized by carboxymethylcellulose (AIS@CMC) were synthesized and functionalized with the cell-penetrating amino acid L-cysteine based on the experimental procedure developed by our group [14]. Briefly, Ag-In-S QDs were synthesized *via* an aqueous route using CMC as capping ligand and metal salts ($AgNO_3$ and $In(NO_3)_3{\cdot}xH_2O$, Sigma-Aldrich) and sulfide ($Na_2S{\cdot}9H_2O$, Sigma-Aldrich) precursors. The main chemical reactions involved are shown in Eqs. (1)–(7). After the dissolution of CMC (Eq. (1)), metal precursor solutions were added (Eqs. (2) and (3)), which formed complexes with CMC macromolecules in solution (Eqs. (4) and (5)). The injection of aqueous sulfide precursor in the medium (Eq. (6)) provoked the nucleation and growth of Ag-In-S almost instantaneously, where the presence of CMC polymer mediated the stabilization (Eq. (7)), reducing surface energy and avoiding further growth. In order to improve the optical properties, Ag-In-S QD colloidal suspension (AIS@CMC) was submitted to thermal annealing treatment (100 ± 5 °C/10 min) to reduce the defects.

$$CMC-COO^-/Na^+{}_{(s)} + H_2O \rightleftharpoons CMC-COO^-{}_{(aq)} + Na^+{}_{(aq)} \quad (1)$$

$$AgNO_{3(s)} + H_2O_{(l)} \rightleftharpoons Ag^+{}_{(aq)} + NO_3{}^-{}_{(aq)} \quad (2)$$

$$In(NO_3)_{3(s)} + H_2O_{(l)} \rightleftharpoons In^{3+}{}_{(aq)} + 3NO_3{}^-{}_{(aq)} \quad (3)$$

$$CMC-COO^-{}_{(aq)} + Ag^+{}_{(aq)} \rightleftharpoons CMC-COO^- - Ag^+{}_{(aq)} \quad (4)$$

$$CMC-COO^-{}_{(aq)} + In^{3+}{}_{(aq)} \rightleftharpoons CMC-COO^- - In^{3+}{}_{(aq)} \quad (5)$$

$$Na_2S_{(s)} + H_2O_{(l)} \rightleftharpoons 2Na^+{}_{(aq)} + S^{2-}{}_{(aq)} \quad (6)$$

$$CMC-COO^- - Ag^+{}_{(aq)} + CMC-COO^- - In^{3+}{}_{(aq)} + S^{2-}{}_{(aq)} \rightleftharpoons Ag-In-S-CMC-COO^-{}_{(colloid)} \quad (7)$$

In the sequence, AIS@CMC QDs were bio-functionalized with L-cysteine amino acid (CYS) based on the EDC chemistry. This nanoconjugate was identified as "AIS-CYS" (AIS@CMC-CYS).

The grafting of AIS-CYS with the mitochondria-targeting peptide (MTP, KLA) was achieved through the conjugation protocol based on EDC/sulfo-NHS chemistry. So, 10.0 mL of AIS-CYS suspension previously prepared was dried in an oven using hot air (at 40 ± 1 °C) to reach a volume of 5.0 mL by solvent evaporation. Then, 200 μL of EDC solution (19 mg/mL in distilled water) was added to the AIS-CYS suspension and stirred for 15 min to activate carboxyl groups of CMC. Under continuous stirring, 5 mL of KLA/sulfo-NHS solution (KLA, 0.2 mg/mL, and sulfo-NHS, 2.2 mg/mL, in phosphate saline buffer, PBS, 2×, pH = 7.4 ± 0.1) solution was added to the flask, and the system was incubated at 6 ± 2 °C for 2 h. The mass ratio of KLA:COO^- from CMC was approximately 1:20 (*w*/w). After the incubation time, the crosslinking reaction was quenched by adding ETA (1.5-fold molar excess to EDC) to the reaction flask and kept under moderate stirring for 10 min. Then, the nanoconjugate was dialyzed for 24 h (with two changes of the dialysate; 4 L of distilled water at pH = 8.0 ± 0.1; NaOH 1 M) using a Pur-A-Lyzer™ Mega Dialysis Kit (Sigma-Aldrich, molecular weight cut-off, MWCO, of 12 kDa) and the final volume reduced to 10 mL by solvent evaporation at 40 ± 1 °C. This MTP-modified quantum dot was identified as "AIS-CYS-KLA" (AIS@CMC-CYS-KLA). A schematic representation of the nanoconjugates is presented in Fig. 1. As a reference, a similar procedure was used to covalently bond KLA to AIS@CMC, forming "AIS-KLA" conjugates.

2.3. Characterization of biofunctionalized hybrid nanoconjugates

Absorption properties of conjugates were obtained using ultraviolet-visible spectroscopy (UV–vis) in transmission mode using Lambda EZ-210 (PerkinElmer). Photoluminescence studies were performed using FluoroMax-Plus-CP (Horiba Scientific) based on steady-state spectroscopy ($\lambda_{excitation}$ = 350 nm), 3D excitation-emission contour plots ($\lambda_{excitation}$ = 250 to 500 nm; $\lambda_{emission}$ = 500 to 800 nm) and time-correlated single-photon (TCSP) for lifetime measurements (Delta-Diode - pulsed laser, $\lambda_{excitation}$ = 375 ± 10 nm, $\lambda_{emission}$ = 625 nm). The fluorescence quantum yields (QY) for nanoconjugates were calculated by using Rhodamine 6G (Sigma-Aldrich) and the comparative method ($\lambda_{excitation}$ = 488 nm). Optical properties were obtained using nanoconjugate suspensions without dilution.

Morphological features and size distribution of inorganic core were evaluated from transmission electron microscopy (TEM, 200 kV, Tecnai G2–20-FEI, FEI Company) coupled with energy-dispersive x-ray spectroscopy (EDX, EDAX detector coupled to Tecnai G2–20-FEI) for evaluation of elemental composition. Samples were prepared by placing the diluted suspension (1:2, suspension:ethanol) on a holey-carbon copper grid.

High-resolution X-ray photoelectron spectroscopy (HR-XPS) spectra were obtained for evaluating oxidation states of AIS QDs using Amicus spectrometer (Mg-Kα; 10 sweeps; Kratos Analytical). Samples were concentrated by centrifugation (Amicon® Ultra Centrifuge Filter, 30 kDa MWCO, Sigma-Aldrich) and the retained materials were poured into plastic molds and dried in a hot-air oven (40 ± 1 °C). Peak positions were corrected based on C 1s adventitious carbon binding energy (284.6 eV).

The occurrence of functionalization with KLA peptide was investigated using Nicolet 6700 Fourier-transform infrared spectrometer (FTIR) in attenuated total reflectance (ATR) mode (4000–850 cm^{-1}, 32 scans; 4 cm^{-1} resolution; Thermo-Fischer). Samples were prepared as described for XPS analysis.

Characterizations using zeta potential (ZP) and dynamic light scattering (DLS) analyses were performed using ZetaPlus instrument (35 mW red diode laser λ = 660 nm, Brookhaven Instruments Corporation) and nanoconjugate suspensions without dilution.

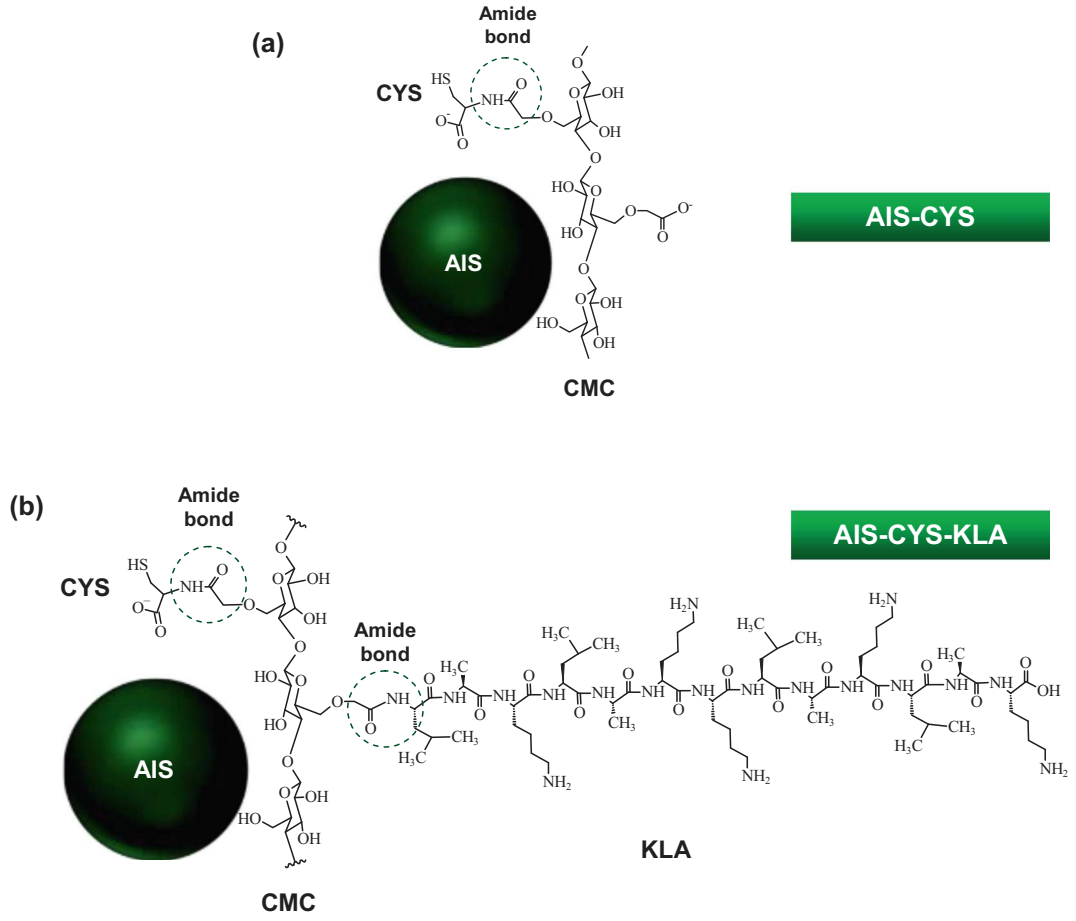

Fig. 1. Schematic representation of (a) AIS-CYS and (b) AIS-CYS-KLA (not to scale).

2.4. Biological characterization of biofunctionalized hybrid nanoconjugates

2.4.1. In vitro assays

Human glioblastoma cells (U-87 MG, ATCC, American Type Culture Collection, HTB-14™, malignant human brain tumors) were purchased from the Rio de Janeiro cell-bank (BCRJ, Brazil) and cultured as previously described by our group [10,13].

2.4.1.1. Bioimaging – cell uptake. The evaluation of the cell-uptake of nanocarriers based on AIS fluorescent green emission was performed by confocal laser scanning microscopy (CLSM) using Eclipse Ti confocal microscope (Nikon Instruments) and FITC fluorescence filter cube ($\lambda_{excitation}$ = 488 nm and $\lambda_{emission}$ = 506–550 nm, typical fluorescein-based dyes and conjugates) as previously reported by our group [10,13]. U-87 MG cells were treated with the nanosystems using two times of incubation (2 h and 6 h).

2.4.1.2. Cell viability. Cytocompatibility assay based on 3-(4,5-dimethylthiazol-2yl-) 2,5-diphenyl tetrazolium bromide, MTT (Sigma-Aldrich), was selected for evaluating the toxicity of AIS-CYS, AIS-KLA, AIS-CYS-KLA, and DOX (doxorubicin hydrochloride, Sigma-Aldrich) as previously reported by our group [10,13,15]. To compare AIS-CYS, AIS-KLA, and AIS-CYS-KLA systems, both nanoconjugates were incubated with U-87 MG cells for 6 h and 24 h at a QD concentration of 3.5 nM and KLA concentration of 0.8 μM (only for AIS-KLA and AIS-CYS-KLA sample, estimated considering the MTP peptide amount added in the functionalization step). To compare the killing activity of AIS-CYS-KLA and DOX chemotherapeutic model drug against U-87 MG cancer cells, MTT tests were conducted by incubating cells for 24 h with KLA (in AIS-CYS-KLA nanoconjugates) and DOX at concentrations of 0.01, 0,05, 0,1, 0,5, 1.0, and 5.0 μM at each well. In this experiment, the cell control group was based on U-87 MG cell culture (GBM) with Dulbecco's Modified Eagle Medium (DMEM) and 10% fetal bovine serum (FBS) (Gibco BRL, USA). Positive control (+ control) was designed using Triton™ X-100 (Sigma-Aldrich), which is the toxic compound to cause cell death (cell culture with DMEM, 10% FBS, and 1.0% *v*/v Triton™ X-100). Negative control (− control) was cell culture with DMEM, 10% FBS and chips of sterile polypropylene Eppendorf®, 1 mg/mL (Eppendorf, Germany), an inert material.

As the cell-killing mechanism of KLA peptide is mostly based on the mitochondrial membrane disruption, to evaluate the cytotoxicity of AIS-CYS-KLA nanoconjugates, mitochondria staining with MitoTracker™ (MitoTracker™ Deep Red FM, Invitrogen™) was also performed. The analysis was conducted by using Eclipse Ti confocal microscope (Nikon Instruments) and TRITC filter cube ($\lambda_{excitation}$ = 543 nm and $\lambda_{emission}$ = 545–645 nm, typical use with tetramethylrhodamine isothiocyanate) after the contact of cells for 15 min and 6 h with the AIS-CYS-KLA nanoconjugates, following the protocols and procedures [10].

2.4.2. Chick chorioallantoic membrane (CAM) assay as an in vivo model

2.4.2.1. Biocompatibility and antiangiogenic activity. Chicken embryo CAM assay was conducted to preliminarily assess *in vivo* antiangiogenic potential and biocompatibility of DOX, AIS-CYS-KLA, and AIS-CYS. Embryonated chicken eggs (*Gallus gallus domesticus*) were incubated under constant humidity and temperature conditions, 65% and 37.0 °C, respectively. On day 3 of egg development, a small window (1 cm^2) was

opened in the eggshell to allow the removal of the inner shell membrane for CAM exposure. The window was sealed with transparent tape, and the eggs were over again incubated. On the fifth day of embryo development, eggs were divided into groups of ten (replicates, $n = 10$), and their CAM's were treated with 50 μL of DOX solution and AIS-CYS-KLA nanoconjugates, both at concentrations of therapeutic agent (DOX or KLA) of 0.01, 0.05, 0.1, and 0.5 μM. Phosphate-buffered saline (PBS) was set as the negative control, and AIS-CYS at the same concentrations of QD used in the AIS-CYS-KLA biofunctionalized sample was used as the reference. After 48 h (day 7 of embryo development) of treatment application, the membranes were photographed at a magnification of 0.67 × .

Using the Angiotool™ software (National Cancer Institute, USA), blood vessels of each membrane were quantitatively analyzed to evaluate the angiogenic response. Blood vessel percentage area, lacunarity, and the total number of intersection points were examined, and the treatment groups' results were confronted with the PBS control group, set to 100%.

2.4.2.2. Glioblastoma growth on CAM. Fertilized chicken eggs (*Gallus gallus dosmeticus*) were incubated at 37 °C and 60% relative humidity until the 9th embryonic developmental day (EDD). On the 9th EDD, a hole of approximately 1 cm^2 was opened in the eggshell to allow the removal of the inner shell membrane for CAM exposure. The window was sealed with transparent tape, and the eggs were over again incubated. On the 11th EDD, the cell culture of 6.0×10^5 U87 cells in 40 μL of ice-cold Matrigel (Corning®, Brazil) was inoculated on CAM next to the largest caliber blood vessel. On the 13th EDD, eggs were divided into groups of six ($n = 6$), and their CAM's were treated with 50 μL of DOX solution and AIS-CYS-KLA at a concentration of 0.5 μM of therapeutic agent (DOX or KLA). Phosphate-buffered saline (PBS) was set as the negative control, and AIS-CYS nanoconjugate at the same concentration of QD in AIS-CYS-KLA was used as the reference. On the 14th EDD of embryo development, the membranes were photographed at a magnification of 0.67×. After the photos, the tumors on CAM were removed and fixed in 10% formaldehyde, dehydrated, and embedded in paraffin. The paraffin blocks were sectioned into 4 μm thick slices, and the tissues were stained with hematoxylin and eosin (H&E).

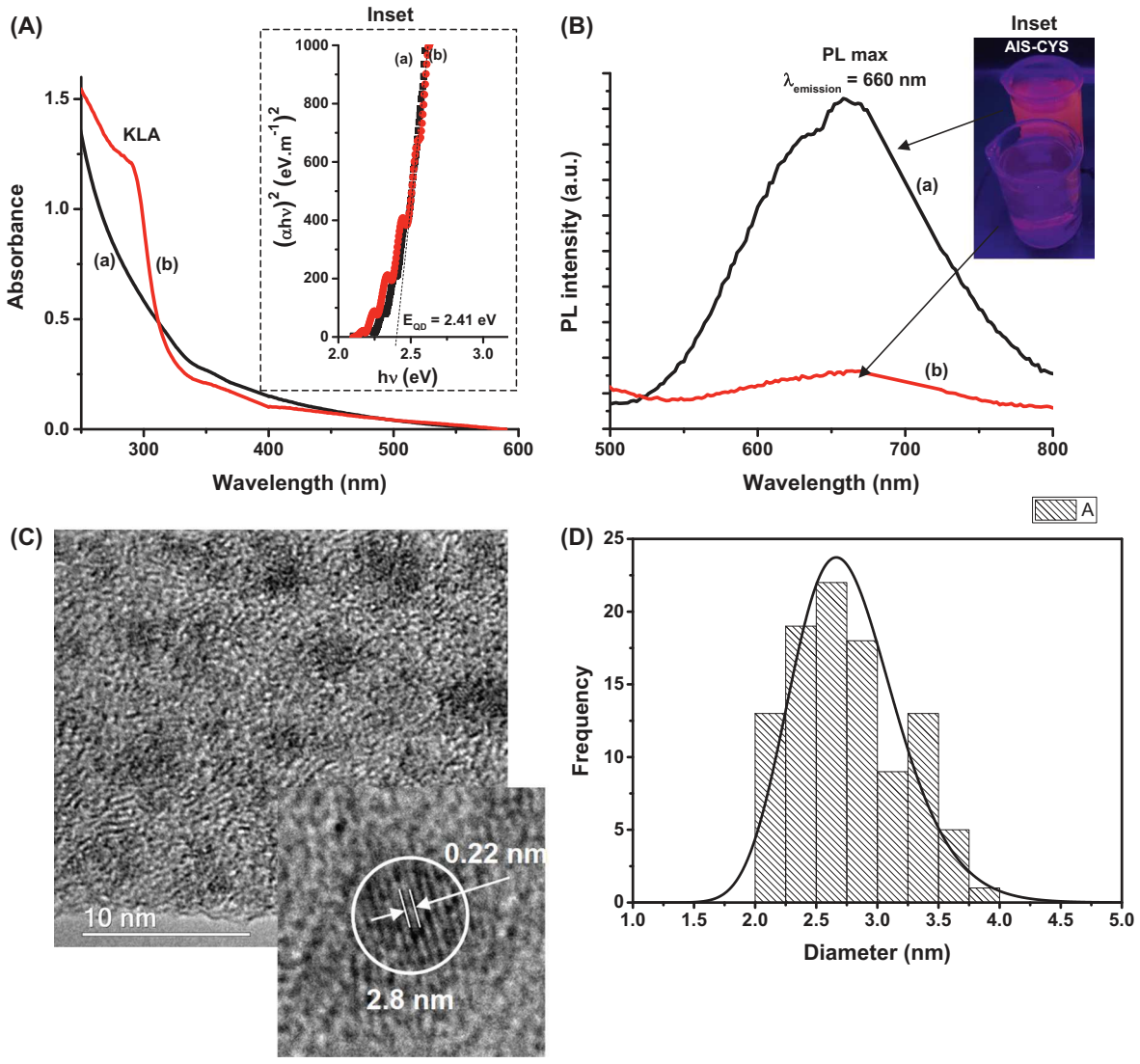

Fig. 2. (A) UV–vis spectra, (Inset: TAUC plot) and (B) photoluminescence spectra ($\lambda_{excitation} = 350$ nm). Inset: images of QDs under UV-radiation ($\lambda_{excitation} = 365$ nm) of (a) AIS-CYS and (b) AIS-CYS-KLA hybrid nanoconjugates. (C) TEM image of AIS-CYS quantum dots surrounded by ligand. Inset: HR-TEM image indicating lattice fringes distance and nanoparticle size. (D) Histogram of the Gaussian size distribution of AIS-CYS inorganic core.

3. Results and discussions

3.1. Characterization of biofunctionalized hybrid nanoconjugates

UV–vis absorption spectra of AIS-CYS and AIS-CYS-KLA conjugates were presented in Fig. 2A. Both AIS QDs showed a relatively broad UV–vis absorption spectrum with an onset at approximately $\lambda = 520$ nm, mainly associated with sub-bandgap states [47]. No significant difference in bandgap energy ($E_{QD} \sim 2.4$ eV) was detected between samples based on *Tauc* plots (*i.e., Tauc plot* is one method of determining the optical band gap in semiconductors) for direct-bandgap [47] semiconductors (Fig. 2A-inset). In addition, the obtained E_{QD} value was higher (*blue-shifted*) than the bulk value of $AgInS_2$ ($E_{bulk} = 1.85$–2.1 eV) [47,48], confirming the effective formation of nanocrystals within the quantum confinement regime (quantum dots). After bioconjugation of AIS-CYS with KLA peptide (Fig. 2A(b)), a clear transition was detected as a shoulder at approximately $\lambda = 290$ nm. According to the literature [49], side chains of charged amino acids (Lys, Arg, Asp, Glu, His) and peptides containing Lys at different separations in the peptide sequence present UV–Vis absorption between 250 and 400 nm due to charge transfer transitions involving the NH_3^+ and COO^- groups of their side chains and the polypeptide backbone.

Photoluminescence spectra (Fig. 2B) revealed the green-near infrared emission range typical of AIS quantum dots with a maximum of intensity (PL max) at 660 nm ($\lambda_{emission}$). This emission is related to defect-related radiative transitions, with full-width at half-maximum (FWHM) of about 400 meV and Stokes shift (estimated as E_{QD}-E_{PLmax}) of 530 meV.

PL emission signal of the AIS-CYS QDs was partially quenched after the covalent conjugation of KLA peptide observed by the changes in spectrum intensity and the digital images under UV light (Fig. 2B-inset). This effect was assigned to the interferences in the charge-carrier separation and energy transfer processes between the excited AIS QD (h^+/e^-, excitonic transition) and the coupled biomolecule (*i.e.,* KLA peptide) upon applying the external irradiation [13,14,24,50]. In this sense, these changes in the absorption and emission properties evidenced the conjugation of mitochondria-targeting peptide (KLA) to AIS-CYS nanosystems.

Morphological and chemical features of the AIS-CYS nanoconjugates were assessed by transmission electron microscopy (TEM) coupled with energy-dispersive X-ray spectroscopy (EDX). A typical TEM image of the AIS-CYS conjugates (Fig. 2C) evidenced the formation of fairly monodispersed spherical nanoparticles. The continuous lattice fringes observed by electron diffraction (high-resolution transmission electron microscopy, HR-TEM, inset image) demonstrated their single-crystalline nature. The interplanar distance of 0.22 ± 0.02 nm is compatible with the (204) diffraction plane of chalcopyrite $AgInS_2$ (JCPDS-International Centre for Diffraction Data, card 32–0483) [51]. The histogram of the nanoparticle size distribution of Ag-In-S inorganic core (Fig. 2D) indicated a lognormal distribution, which is characteristic of nanoparticles [52], with an average size of 2.7 ± 0.4 nm. This result endorsed the formation of nanoparticles in the quantum size regime as the Bohr diameter ($2R_{Bohr}$) of $AgInS_2$, consistent with the literature reported by Torimoto et al. (2012) as 7.2–7.3 nm [53] and by Hamanaka et al. (2011) as 11.0 nm [54]. EDX measurements showed the presence of Ag, In, and S as predominant chemical elements of the QDs (Fig. S1). Additionally, chemical elements C, O, and Na (sodium salt form) were also detected in the EDX spectra from the CMC polymer ligand. The copper (Cu) and silicon (Si) elements are associated with the grid used as solid support for sample deposition and the microscope detector, respectively.

Moreover, a high-resolution X-ray photoelectron spectroscopy (HR-XPS) analysis was also performed to assess the oxidation states of the chemical elements of the AIS inorganic core (Fig. S2). The XPS spectrum of the Ag 3d region revealed a doublet at 373.7 eV (Ag $3d_{3/2}$) and 367.8 eV (Ag $3d_{5/2}$) that was assigned to Ag (3d) transitions in Ag^+, evidencing a spin-orbit splitting of 5.9 eV. Regarding the In 3d region, the peaks at 452.0 eV and 444.4 eV match the $3d_{3/2}$ and $3d_{5/2}$ levels, respectively, typical of In^{3+} transitions. A binding energy interval of 7.6 eV separated the spin-orbit components. Moreover, S 2p signals displayed two overlapped peaks, 162.6 eV (S $2p_{1/2}$) and 161.4 eV (S $2p_{3/2}$), with energy differences of $\Delta = 1.2$ eV, characteristic of sulfides (S^{2-}) [47].

In addition to optical, morphological, and compositional properties, surface chemistry characterization and the supramolecular conformation of the colloidal nanostructures plays a pivotal role in applications in the biomedical field. Thus, Zeta potential (ZP) and dynamic light scattering (DLS) analyses were performed. CMC polymer at pH = 7.0 possesses a ZP value of about – 50 mV that agrees with the presence of carboxylate (COO^-) species above pKa ($\sim$ 4.5). Upon the formation of AIS QD and functionalization with L-cysteine, a significant lowering of ZP was observed ($ZP = -18 \pm 1$ mV) as a consequence of the overall balance of the conformation of CMC ligand surrounding the QDs, the consumption of carboxylates groups upon conjugation with CYS amino acids, and the addition of a negative charge from deprotonated amino acid. After biofunctionalization with KLA, despite the introduction of a positively charged peptide chain (isoelectric point ~11, simulated using PepCalc.com, Innovagen AB) and the reduction of anionic groups of CMC, associated with the formation of amide bonds, only a slight reduction in ZP was measured (-13 ± 1 mV). This behavior may be interpreted based on the overall geometry of molecules after the EDC-based conjugation reaction. It should be noted that the ZP values measured for both conjugates were in the range where steric hindrance is assumed as the primary mechanism of nanosystem stabilization. The DLS analysis gives information regarding the size (hydrodynamic diameter, D_H) of the nanoconjugate colloidal suspensions. D_H is the sum of the contributions of the inorganic core and the organic shell and its interaction with the surrounding aqueous medium. A D_H of 66 nm (PDI = 0.247) was calculated for AIS-CYS and, after covalent bonding with KLA (AIS-CYS-KLA), a significant increase of about 110% ($D_H = 139$ nm, PDI = 0.311) was detected, as a result of a new supramolecular colloidal structure. Fig. 3A summarizes the surface chemistry and supramolecular features of the supramolecular nanocolloids.

The structural characterization by infrared spectroscopy (FTIR) was performed to evaluate the changes in the CMC polymer compared to AIS-CYS and AIS-CYS-KLA nanoconjugates. In all of the spectra (Fig. 3B), the typical bands of CMC capping ligand related to carboxylate/carboxylic (–COO^-/–COOH), hydroxyls (-OH), methylene (-CH_2), alcohols (C-OH), and β1–4 glycoside bonds were detected [12,13]. The grafting of CMC (Fig. 3B(a)) with CYS in AIS-CYS (Fig. 3B(b)) nanoconjugates and of KLA in AIS-CYS-KLA (Fig. 3B(c)) was mainly identified by the presence of the vibrations of Amide *I* band (mostly ν C=O) at 1650 cm^{-1}, Amide II (δ NH and ν CN) at 1530 cm^{-1}, and Amide III (in-plane δ NH and ν CN) at 1240 cm^{-1}. Amide bonds were formed between carboxylate groups of CMC and amine groups of CYS or KLA based on the EDC-chemistry process through chemical functionalization. The IR band associated with the thiol side groups ($\sim$ 2550 cm^{-1}) of cysteine is frequently very weak, and so, it is scarcely observed by FTIR. For AIS-CYS-KLA nanoconjugate, after conjugation, the presence of unreacted amine ($-NH_2$) groups in lysine amino acid residues was recognized by the significant increase of absorbance at 3000–3300 cm^{-1} and at 1555 cm^{-1} associated with νNH and δNH vibrations, respectively. The relative intensification in the absorbance values also detected at 2900–3000 cm^{-1} was assigned to νCH_3 groups present in alanine and leucine amino acids of KLA peptide [55].

3.2. Biological experiments with biofunctionalized hybrid nanoconjugates

3.2.1. In vitro tests

3.2.1.1. Bioimaging – cell uptake. Bearing in mind the potential use of AIS-CYS and AIS-CYS-KLA nanobioprobes for fluorescent bioimaging of

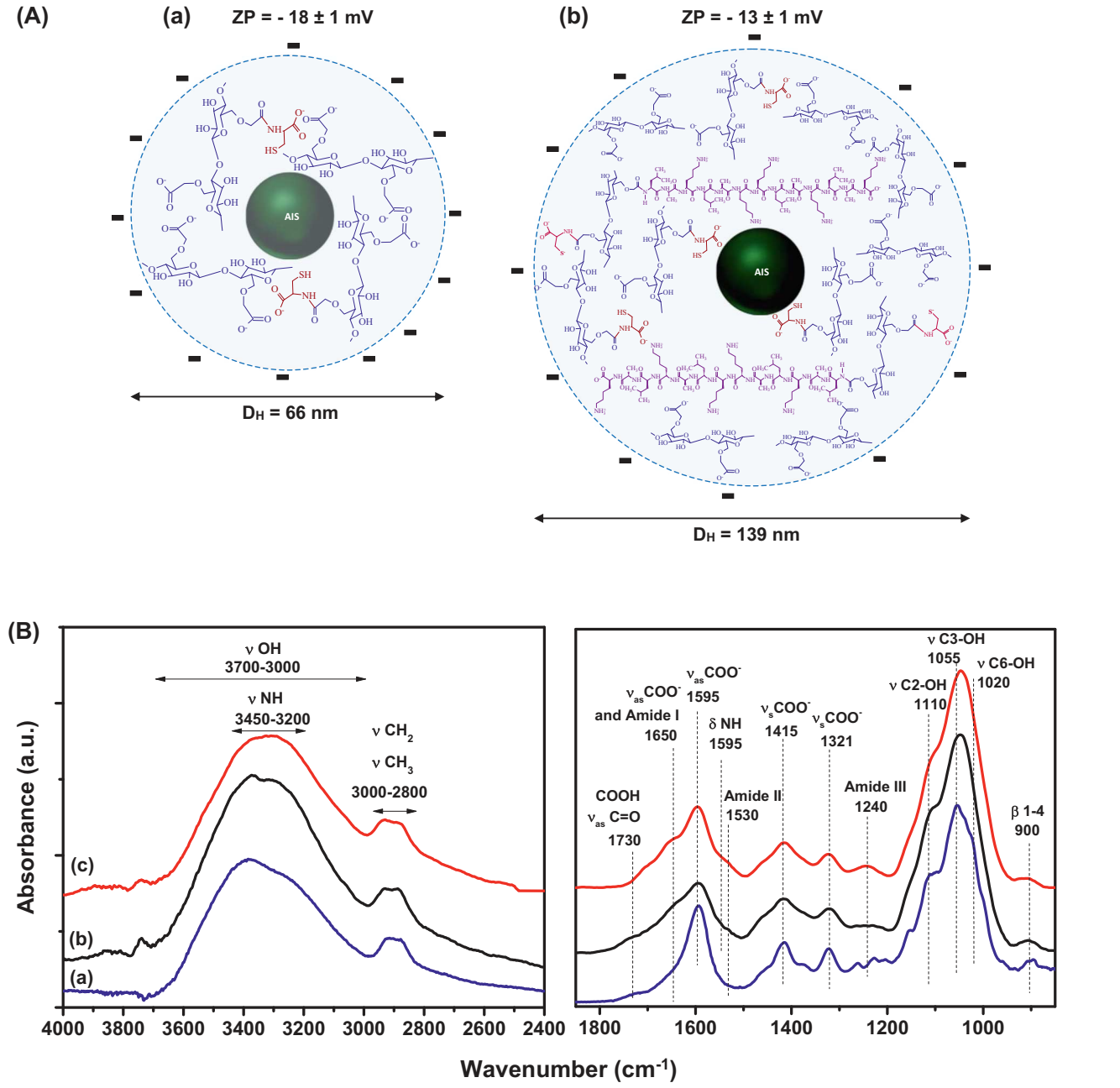

Fig. 3. (A) Schematic representations of surface chemistry and supramolecular nanostructures of (a) AIS-CYS and (b) AIS-CYS-KLA (not to scale). (B) FTIR spectra of (a) CMC, (b) AIS-CYS, and (c) AIS-CYS-KLA.

tumor cells, the characterization was performed through a 3D excitation-emission plot, lifetime measurements, and quantum yield evaluation. The typical result of 3D contour curves for the AIS systems (Fig. 4A) revealed emissions in the visible range from green to red over a wide range of excitation, which is appropriate for bioimaging. The values of intensity averaged lifetimes (τ_{av}) obtained for AIS-CYS (312 ± ns) and AIS-CYS-KLA (211 ± ns) confirmed the significant contribution of electron-hole recombination mechanisms based on defect points/intra-bandgap levels that are longer than band-to-band recombination. These results are much higher than those typically observed for organic fluorophores (<10 ns) [56]. These lifetimes favor bioimaging applications due to better temporal separation of the QD signals from cellular auto-fluorescence, boosting bioimaging sensitivity [56], as well as permitting long-term tracking in biological studies [57]. Additionally, the quantum yield (QY) of AIS quantum dots was measured, showing a QY = 0.6% for AIS-CYS and 0.1% for AIS-CYS-KLA, which has already proven suitable to be used as quantum dot-based fluorophores for bioimaging applications [58] and consistent with the literature regarding QD produced by aqueous colloidal low temperatures routes [18,21]. This characteristic was confirmed by the confocal scanning microscopy images (CLSM) of GBM cancer cells (U-87 MG) after incubation for 2 h and 6 h with AIS-CYS (Fig. 4B(a)) and AIS-CYS-KLA (Fig. 4B(b)) nanoconjugates. QD internalization by the brain cancer cells was distinguished by the green fluorescent emission of AIS QDs under laser excitation, which is absent in control samples (without incubation with quantum dots). The fluorescent emission was predominantly observed scattered in the cytosol without accumulation in the cell nucleus, allowing for intracellular bioimaging and cell tracking. Thus, these features offer the possibility of using the nanoconjugates for diagnosis applications and assessing mechanisms of targeting and killing cancer cells *in vitro*.

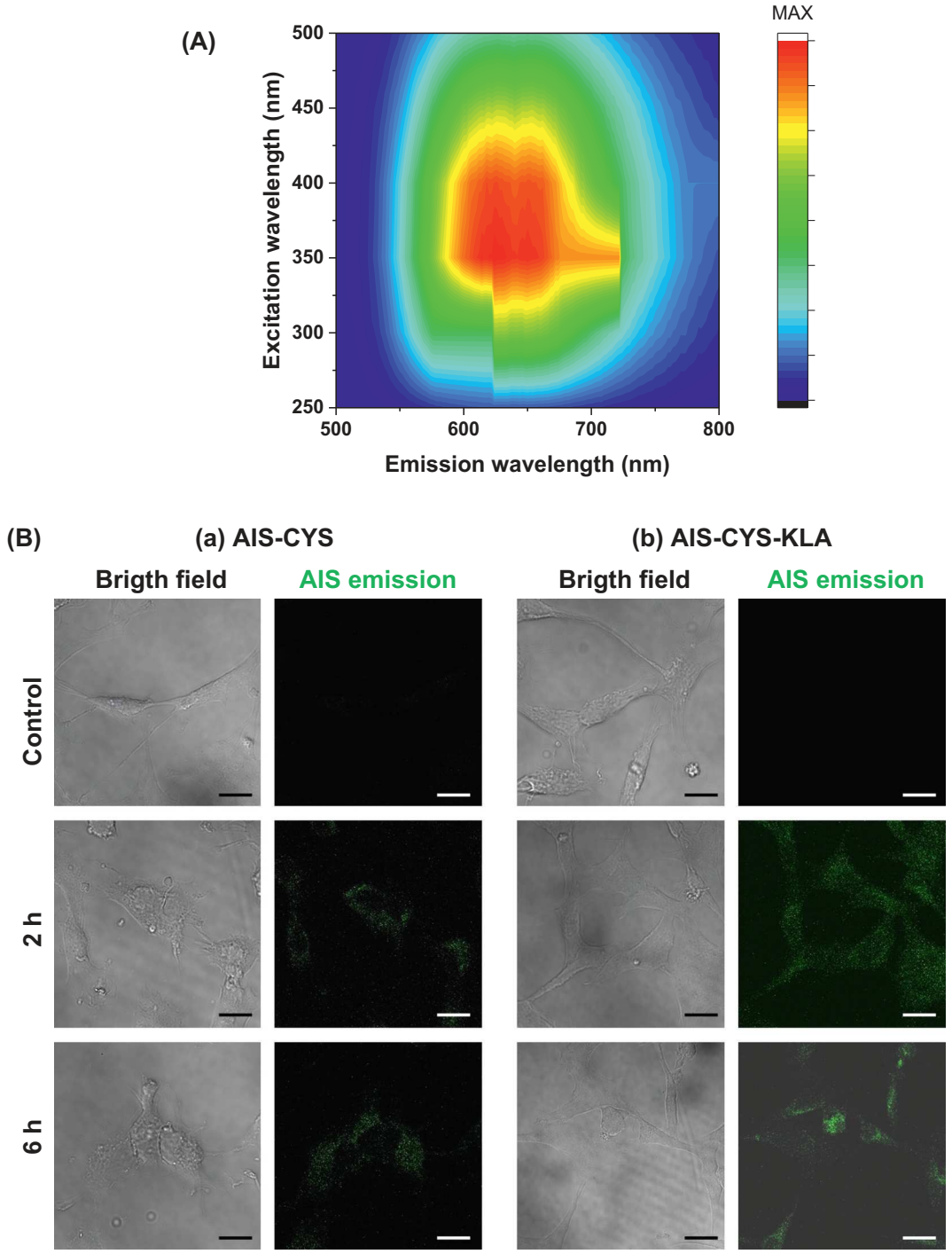

Fig. 4. (A) Typical excitation-emission contour plot of AIS QDs stabilized by CMC used in this study; (B) CLSM images of U-87 MG cancer cells after incubation with (a) AIS-CYS and (b) AIS-CYS-KLA after 2 h and 6 h in comparison to control (no quantum dots) (FITC channel, scale bar = 10 μm).

3.2.1.2. Cytotoxicity assays. The cytotoxicity results for AIS-CYS compared to AIS-CYS-KLA are summarized in Fig. 5A. As anticipated, the AIS-CYS sample was non-toxic to cancerous cells (cell viability >90%), which was ascribed to the inherent biocompatibility of the CMC biopolymer and L-cysteine amino acid as well as the minor toxicity of AIS QDs (core). In addition, no significant difference (ANOVA One Way, Bonferroni Test, level of significance, $\alpha = 0.05$) was observed between the two incubation times, indicating that no toxicity was verified even for longer times. These findings give additional proof of the potential application of the nanosystems as biomarkers and drug nanocarriers in future clinical translation for cancer nanotheranostics. That could indicate a longer circulation time in the body after administering the nanomedicine without eliciting significant toxicity or side effects.

Conversely, KLA peptide covalently bonded to nanoconjugates (AIS-KLA and AIS-CYS-KLA) reduced the cell viability. The cell viability of cells in contact with AIS-KLA was 80% and 76% after 6 h and 24 h of incubation, respectively, compared to 57% (6 h) and 52% (24 h) observed for the AIS-CYS-KLA. These results showed that AIS-CYS-KLA nanosystems are considered cytotoxic (*i.e.,* cell viability <70%) and that, based on statistical analysis (ANOVA One Way, Bonferroni Test), for the AIS-CYS-KLA ($\alpha = 0.01$) and AIS-KLA ($\alpha = 0.05$), the results are significantly different when comparing incubation times of 6 h and 24 h.

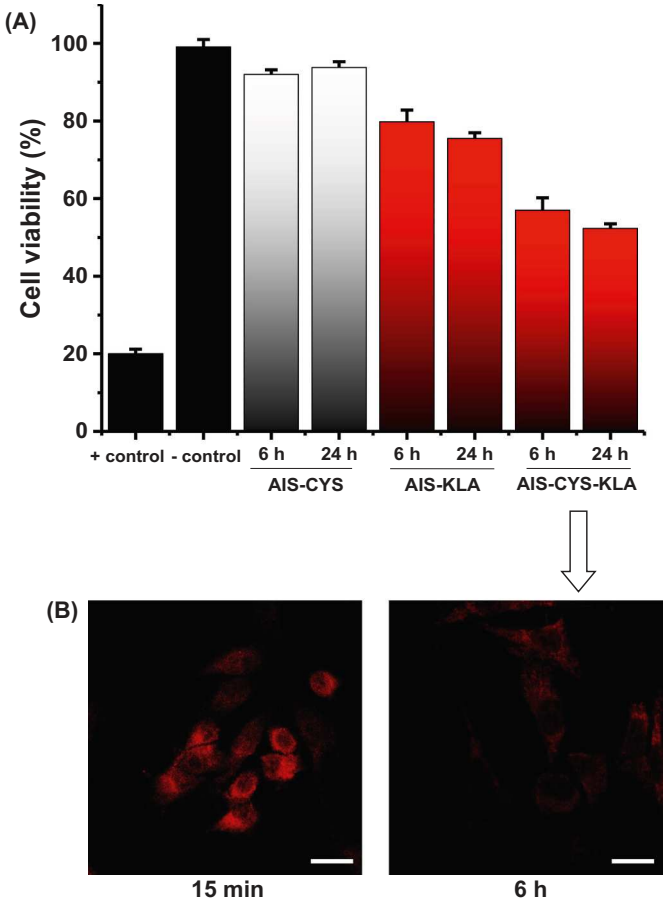

Fig. 5. (A) Cell viability responses of AIS-CYS, AIS-KLA, and AIS-CYS-KLA after incubation for 6 h and 24 h with U-87 MG cell line and [peptide] = 0.8 μM (n = 6); (B) CLSM images of U-87 MG cells after incubation for 15 min and 6 h with AIS-CYS-KLA to evaluate red emission of MitoTracker™ (TRITC channel, scale bar = 10 μm). (For interpretation of the references to colour in this figure legend, the reader is referred to the web version of this article.)

That means, although relevant effects of KLA (*i.e.,* mitochondria-targeting peptide) cytotoxic were already observed for the first 6 h, the nanoconjugates maintained cytotoxic by reducing the cell viability up to 24 h of incubation. These results also evidenced that the grafting -CYS functionality conjugated with CMC ligand showed a *boosting* effect on the cytotoxicity of the bioconjugates with a reduction of cell viability higher than 30% after 24 h. The cellular uptake of AIS-CYS-KLA nanoconjugates may have triggered the therapeutic activity of the KLA peptide based on mitochondrial dysfunction pathways [1,32–35]. Thus, although KLA pro-apoptotic peptide possesses poor cell membrane permeability, this cytotoxic behavior was credited to the capability of this innovative nanocarrier of CMC polymer modified with L-cysteine to facilitate cellular internalization. The thiolation of CMC with L-cysteine (*i.e.,* thiol-bearing biomolecule) in the bioconjugates was designed as cell-penetrating moiety for augmenting KLA internalization. A similar trend has been reported for cell-surface thiol-bearing biomolecules that actively intermediate the cellular internalization processes through the dynamic balance of redox species (SH/S-S) [59–61]. Although the exact mechanism is still unidentified, the most accepted concepts encompass the formation of disulfide complexes involving thiol moieties from the delivery nanoagents and the cell membrane (*i.e.,* balance of oxidized/reduced species) at the bio-interfaces. In the sequence, the internalization of the complex takes place, and, at the last stage, the payload is released within the cytosol environment [59–61]. However, it is still a matter of intensive research regarding the specific activity of cysteine residues in affecting cell-death mechanisms and pathways, besides the already recognized effect of a cell-penetrating agent. It should be noted that the AIS-KLA (without CYS) also acted as a vehicle for intracellular delivery of the KLA, due to the presence of CMC, even on a minor scale compared to the thiol-based-cell-penetrating agent. This effect regarding the cell uptake of CMC-stabilized nanostructures was already well established [12,13,24,58].

In addition to the MTT test, considering that the major cell-killing mechanism of KLA-based peptides involves the mitochondrial membrane disruption, the *in vitro* toxicity of nanoconjugates was evaluated by MitoTracker™ biomarker based on the mitochondria staining method. Thus, as actively functional mitochondria concentrate this dye fluorophore (MitoTracker™), it was used to track the action of KLA-modified hybrid nanocarriers. Hence, GBM cells (U-87 MG) were incubated with the labeled nanoconjugates (MitoTracker™ Deep Red FM) and analyzed using confocal laser scanning microscopy (Fig. 5B). In a general view, the fluorescence confocal images showed a significant reduction of the red emission with the incubation time, assuring the mitochondria dysfunction provoked by KLA peptides conjugated to the nanohybrid nanosystems consistent with the MTT cell viability findings of the previous section.

To validate that the triggering of cell-death induction by the pro-apoptotic KLA peptide was concentration-dependent, different concentrations of AIS-CYS-KLA conjugate were tested (Fig. 6, from 0.01 to 5.0 μM). The results validated the death-inducing activity of KLA, the cell-penetrating action of CYS residues, and the enhanced lethality by grafting KLA peptides to the nanoconjugates. For comparison with a model anticancer drug, the same concentrations of DOX were added to GBM cancer cells. The results indicated that, for concentrations of KLA and DOX below 0.1 μM, the lethality of KLA-modified nanoconjugates was approximately 23–36% higher than DOX. The killing activities of both systems (*i.e.,* DOX and nanohybrids) were similar to the other concentrations. These results are outstanding for developing new anticancer agents once it permits decreasing the therapeutic dosages while maintaining the killing effectivity against cancer cells. Consequently, these *smart* nanoconjugates would prevent the generally observed adverse collateral effects associated with high doses of anticancer drugs that are often administered to patients in conventional chemotherapy [17].

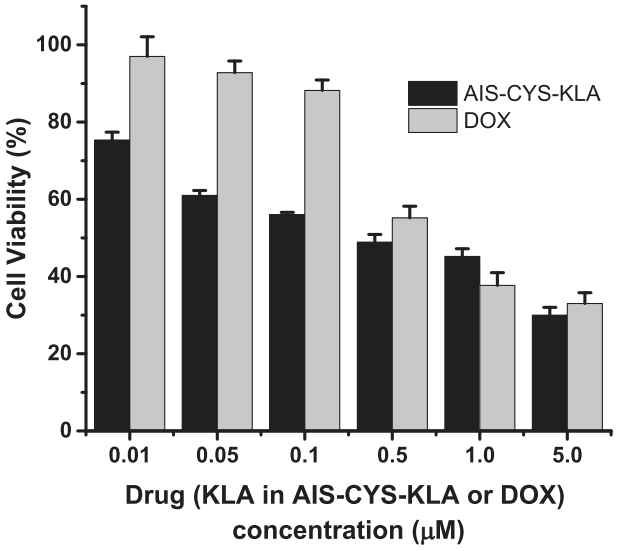

Fig. 6. Cell viability responses comparing the AIS-CYS-KLA nanoconjugates and DOX chemotherapeutic agent (n = 6).

3.2.2. Chick chorioallantoic membrane (CAM) assay as an in vivo model

3.2.2.1. Biocompatibility and antiangiogenic activity. Chicken embryo CAM assay was conducted to preliminarily assess *in vivo* antiangiogenic potential and biocompatibility of DOX, AIS-CYS-KLA, and AIS-CYS. Fig. 7 shows representative images of the CAM after treatment with PBS (negative control), AIS-CYS (reference), DOX and AIS-CYS-KLA at 0.01, 0.05, 0.1, and 0.5 μM of therapeutic agent (DOX or KLA). The results obtained for the groups treated with AIS-CYS were similar to those from the control group (PBS). Conversely, the sample groups treated with DOX and AIS-CYS-KLA demonstrated a significant reduction in the CAM vessels.

To confirm the qualitative data observed in Fig. 7, the area of the vessels, the number of junctions, and lacunarity were measured (Fig. 8). AIS-CYS at 1.2 nM of AIS showed a small but significant reduction in vessel area (21%). Although AIS-CYS treated groups did not lead to a statistical reduction in vessel area, a lower number of junctions (* ~ 33%) than the PBS group was observed. Antiangiogenic activity of AIS-CYS-KLA was confirmed by quantification of the blood vessel area. AIS-CYS-KLA demonstrated antiangiogenic activity, with reduction of percentage of vessels of 32% (0.01 μM), 30% (0.05 μM), 30% (0.1 μM), and 27% (0.5 μM). The vessel percentage area presents a reduction similar to the positive control (DOX) (23% at 0.01 μM). As expected, a decrease in the vessels' number of junctions at the same levels of DOX 0.01 μM (34%) was observed in AIS-CYS-KLA treated groups at 0.01 μM (45%), 0.05 μM (34%), 0.1 μM (29%), and 0.5 μM (45%). Moreover, AIS-CYS-KLA treated groups increased lacunarity (>100%) at all tested concentrations. This disorder was only for the group that received DOX at 0.5 μM.

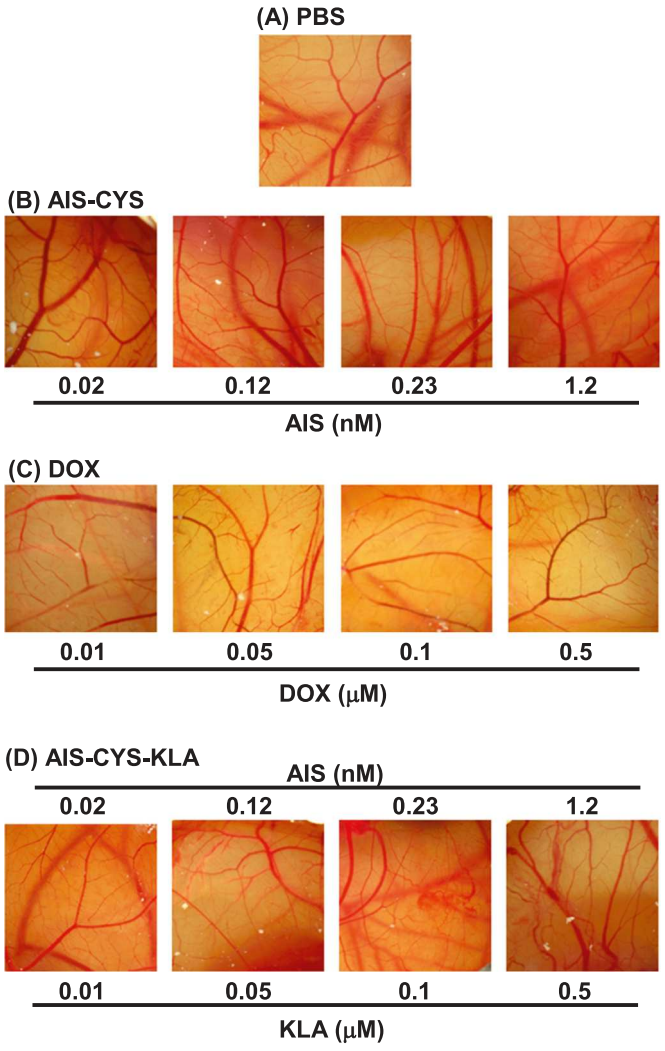

Fig. 7. Representative photographs of CAM after 48 h (day 7 of embryo development) of treatment with (A) PBS (negative control), (B) AIS-CYS (reference), (C) DOX, and (D) AIS-CYS-KLA at therapeutic agents (DOX or KLA) concentrations of 0.01, 0.05, 0.1, and 0.5 μM (n = 10; 0.67× magnification).

Angiogenesis is a process that involves the formation of blood vessels from pre-existing vessels, which can occur under physiological and pathological conditions. Neovascularization is crucial for the development of tumor cells because it contributes to the growth and proliferation of the tumor, and glioblastomas have a rich network of vessels [62,63]. Therefore, recent studies have developed therapeutic strategies to reduce angiogenesis in treating these tumors [64,65]. Our study demonstrated the antiangiogenic activity of AIS-CYS-KLA in the chicken embryo CAM assay. The evaluated concentrations of AIS-CYS-KLA showed a significant reduction in the vessels, similar to doxorubicin [66–69].

In addition, the CAM assay is a valuable tool to pre-screening the biocompatibility of different biomaterials [70]. No signs of toxicity such as lysis, bleeding, and clotting, or acute inflammatory response, were observed; thus, we can conclude AIS-CYS and AIS-CYS-KLA, in the analyzed concentrations, were non-toxic under the investigated conditions.

3.2.2.2. Glioblastoma growth on CAM. In our work, CAM tumor assay was used to assess the anti-tumor effect of AIS-CYS-KLA. Because it has an immature immune system until the 14th embryonic developmental day, CAM has been used successfully as a tumor growth model from a cell suspension or graft tumor explants. Besides that, it presents a favorable microenvironment for tumor development, and it allows tumor evaluation cell invasion, angiogenesis, and expression of signaling molecules [71,72]. After the growth of the glioblastoma tumor in the CAM, the membranes were treated with PBS (negative control), AIS-CYS, DOX, and AIS-CYS-KLA.

The negative control (PBS) showed a white mass consistent with tumor growth (Fig. 9A(a)). The group that received AIS-CYS (1.2 nM of AIS, Fig. 9B(a)) did not show a tumor reduction and did not present vascular changes such as hemorrhages, thrombosis, fibrosis, or even destruction of the CAM. The group treated with DOX (0.5 μM, Fig. 9C(a)) morphologically showed a reduction in the tumor white mass, but it was not statistically significant. In addition, some membranes of this group showed bleeding points. The AIS-CYS-KLA treated group (0.5 μM, Fig. 9D(a)) showed a statistically significant reduction in tumor white mass ($p = 0.0087$) when compared with the other groups (Fig. 9 - inset). The area of the tumor was significantly reduced (41%) in the AIS-CYS-KLA group when compared with the vehicle (no reduction), and a better reduction than the DOX-treated group (35%). Thus, it is suggested that AIS-CYS-KLA can be a potential treatment for tumor glioblastoma.

Glioblastoma U-87 MG cells treated with PBS solution were able to grow on CAM (Fig. 9A(a-e)). Histological analyzes of the membrane revealed the presence of two main cell subpopulations (P1 and P2), necrotic areas that are usually seen in acellularity pattern (ne), in the tumor formed by the grafted (Fig. 9A(b)). The presence of necrosis is one of the histologic characteristics of glioblastoma. We also observed glomeruloids with microvascular endothelial proliferation (MV) within the CAM (Fig. 9A(d-e)). After exposure to treatment with AIS-CYS suspension (1.2 nM of AIS), we observed the growth of a tumor with three distinct cell populations, with an extensive CAM invasion region (Fig. 9B (b-c)).

AIS-CYS samples (Fig. 9B(d)) showed a disorganized tissue by the presence of CAM extensive invasion forming lacunar structures that intertwine between tumor and CAM tissue. After treatment of DOX (0.5 μM, Fig. 9C(b-e)), the presence of the region of invasion of the tumors

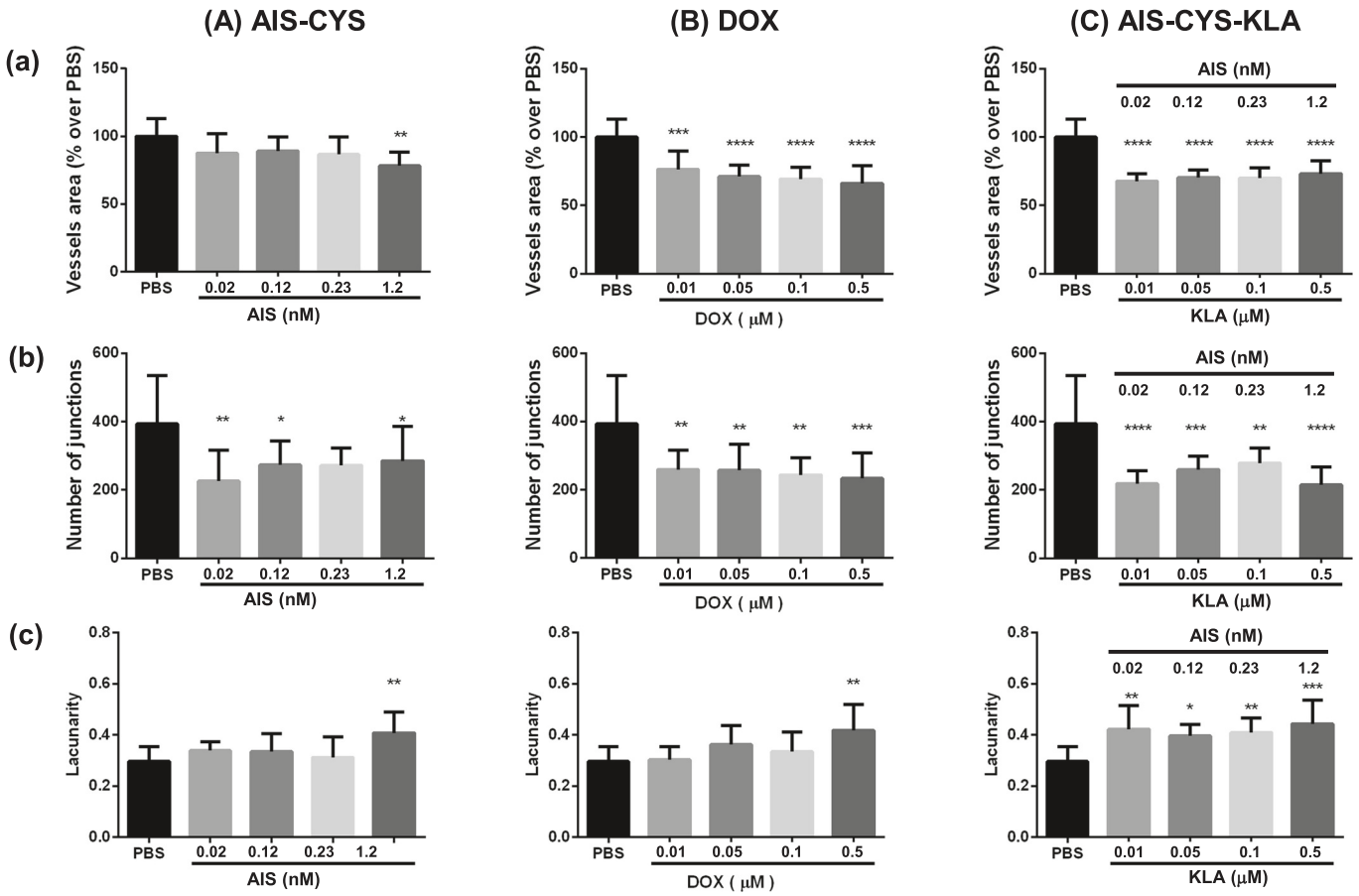

Fig. 8. Graphs show the (a) vessel area (%), (b) the number of junctions, and (c) lacunarity after treatment with PBS (negative control, black columns), (A) AIS-CYS (reference), (B) DOX, and (C) AIS-CYS-KLA at therapeutic agents (DOX or KLA) concentrations of 0.01, 0.05, 0.1, and 0.5 μM. Treatment groups were compared with the PBS group, set to 100%. The data are represented by mean ± standard deviation (SD) (n = 10). *Significant difference compared with PBS group (*$p < 0.05$, **$p < 0.01$, ***$p < 0.001$, ****$p < 0.0001$).

was observed on CAM (yellow arrows, Fig. 9C(c)). We observed in higher magnification the presence of glomeruloids appearing in microvascular proliferation clusters (MV) within the CAM (Fig. 9C(e)). The treatment with AIS-CYS-KLA (0.5 μM) showed glomeruloids appearing in microvascular proliferation clusters (MV) within the CAM (Fig. 9D(b-c)). Fig. 9D(d) showed an extensive area of the tumor formed three subpopulations morphologically distinct and a clear delimitation between the tumor and the CAM (dotted red lines). Both samples showed clusters of tumor cells within the CAM.

Histological analysis of some glioblastoma samples that received the AIS-CYS-KLA treatment showed the presence of some histologic hallmarks of glioblastoma, such as structures similar to glomeruloid vessels and the presence of three subpopulations morphologically distinct from the tumor [73,74]. The presence of typical features of glioblastoma in tumors developed on CAM reinforces the importance of this *in vivo* assay as a valuable tool for the preliminary assessments of the efficiency of GBM targeted therapy responses for the development of new treatments [75]. These histopathological features were also found in the PBS, AIS-CYS, and DOX samples. However, the PBS (negative control) presented disorganized tissue by the presence of CAM extensive invasion forming lacunar structures that intertwine between tumor and CAM tissue. In contrast, the three subpopulations showed a clear delimitation between the tumor and the CAM when treated with AIS-CYS-KLA. When analyzed together, the results of tumor size and histopathological analysis suggest that treatment with AIS-CYS-KLA is a promising alternative for the treatment of glioblastoma. Thus, compared to the mouse animal model, the CAM *in vivo* assay can be considered a viable alternative [76]. Nonetheless, despite all these advantages, the CAM assay is not endorsed to be directly applied as a model for simulating the unique features of the blood-brain barrier (BBB), which is far more complex, considerably limiting the effectiveness of advanced nanocarriers as anticancer drug delivery systems [5,77]. Therefore, a comprehensive investigation of BBB transposing by these nanohybrids would require more profound research, with additional experiments, such as the bEnd3 endothelial cells model derived from mouse brain *in vitro* assay [78], which is beyond the main scope of the current study. It will undoubtedly be considered for future studies in the development process of these hybrid supramolecular nanosystems before the clinical trial, including innovative escaping alternatives to surpass the BBB (*e.g.,* nose-to-brain delivery) for evaluating anticancer drugs, as recently reported [79,80].

Hence, based on these results and the important considerations highlighted, the CAM *in vivo* model satisfies the current requirements, which should be relatively rapid, cost-effective, and "3Rs" compliant to support the identification of new prospective cancer nanotheranostics. In this sense, they would possibly progress to practical preclinical/clinical trials and, more importantly, demonstrate a substantial antineoplastic action against glioblastoma cancer cells.

The complete representation of the nanosystem successfully designed, produced, and comprehensively characterized through *in vitro* and *in vivo* bioassays in this research is depicted in Fig. 10.

4. Conclusions

We designed, produced, and comprehensively characterized innovative nanohybrids composed of peptide-functionalized carboxymethylcellulose as a macromolecular-based shell conjugated with a

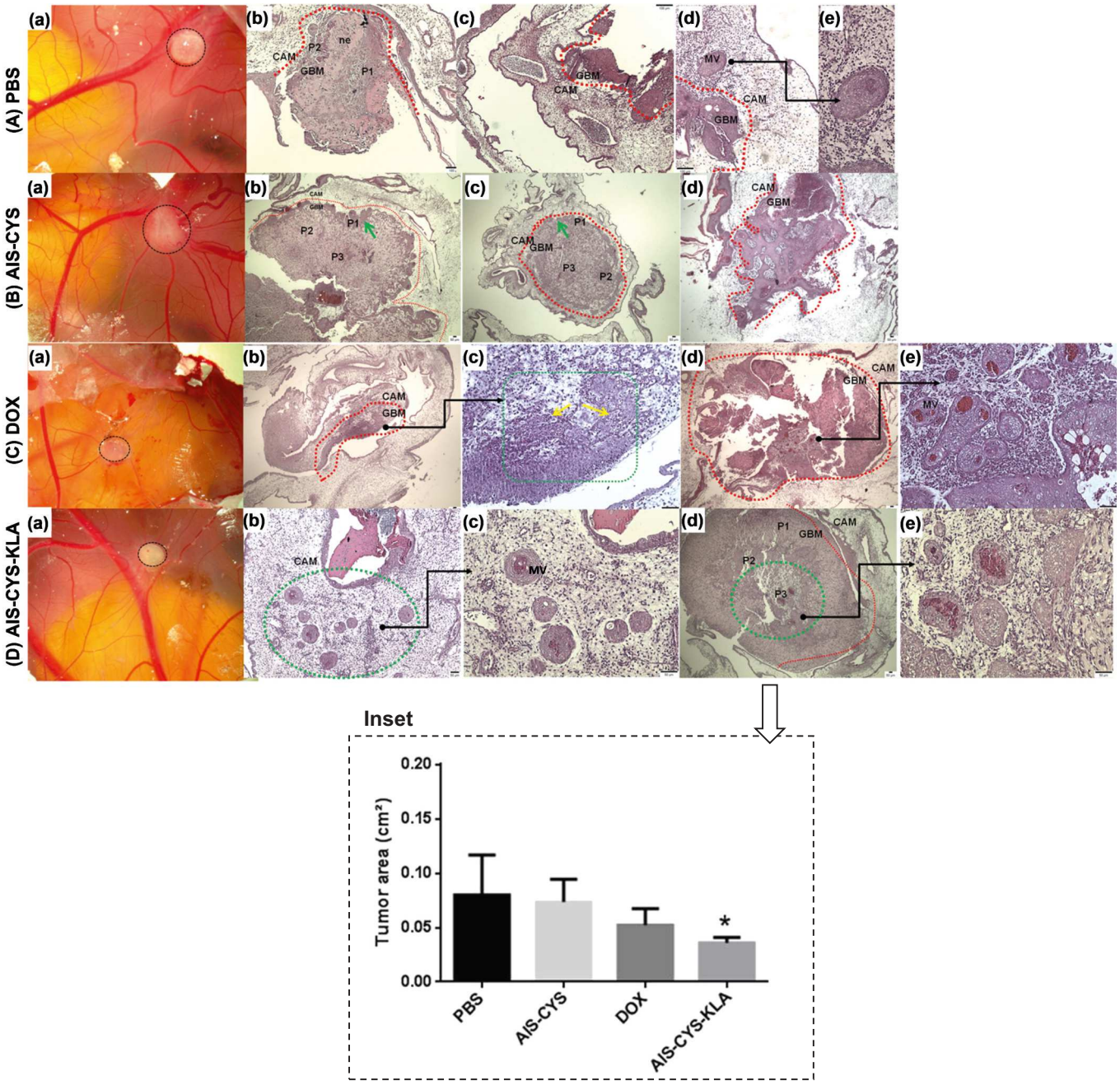

Fig. 9. Representative photographs of glioblastoma growth on CAM on the 14th EDD of embryo development (a) and histological analysis of longitudinal sections of CAM after 24 h of treatment with (A) PBS 1×, (B) AIS-CYS, and (C) DOX and (D) AIS-CYS-KLA (DOX or KLA at 0.5 μM). (b-e) Different cell subpopulations morphologically distinct between tumors formed are indicated by P1, P2, P3; GBM (tumor); CAM (chorioallantoic membrane); Glomeruloids appearing in microvascular proliferation clusters (MV); dotted red line (region of cell transition between the tumor and the CAM); green arrows (extensive CAM invasion); yellow arrows (presence of the area of invasion of the tumors on CAM). Macroscopic aspects: 0.67× magnification. Inset: The graph shows the tumor area (cm^2) after treatment with PBS (negative control), AIS-CYS (reference), and DOX and AIS-CYS-KLA at therapeutic agents (DOX or KLA) concentrations of 0.5 μM. The data are represented by mean ± SD ($n = 6$). *Significant difference compared with PBS group ($^*p < 0.05$). (For interpretation of the references to colour in this figure legend, the reader is referred to the web version of this article.)

fluorescent Ag-In-S semiconductor quantum dot (AIS QD) core. These nanosystems were synthesized through a strictly *green* chemistry process. These hybrid supramolecular nanosystems were successfully biofunctionalized with L-cysteine amino acid (CYS) as the cell-penetrating moiety combined with KLA peptide as mitochondria-targeted pro-apoptotic agent for potential application in brain cancer nanotheranostics. *In vitro* assays demonstrated that, before grafting KLA peptides, they were non-toxic and suitable for glioblastoma cell bioimaging assessed through fluorescent microscopy analysis. Notably, the grafting of CYS amino acid combined with KLA peptide (AIS-CYS-KLA) was highly active in enhancing the nanohybrids' cellular internalization and radically boosting their lethality towards brain cancer cells relying on targeting mitochondrial dysfunction. Through the *in vitro* cytotoxicity assays, the nanohybrids proved to be more effective in killing brain cancer cells than "free" DOX, used as a model anticancer drug. Moreover, these results were corroborated by *in vivo* chicken embryo CAM assay. Our study demonstrated the antiangiogenic activity of AIS-CYS-KLA nanosystems based on the significant reduction in the blood

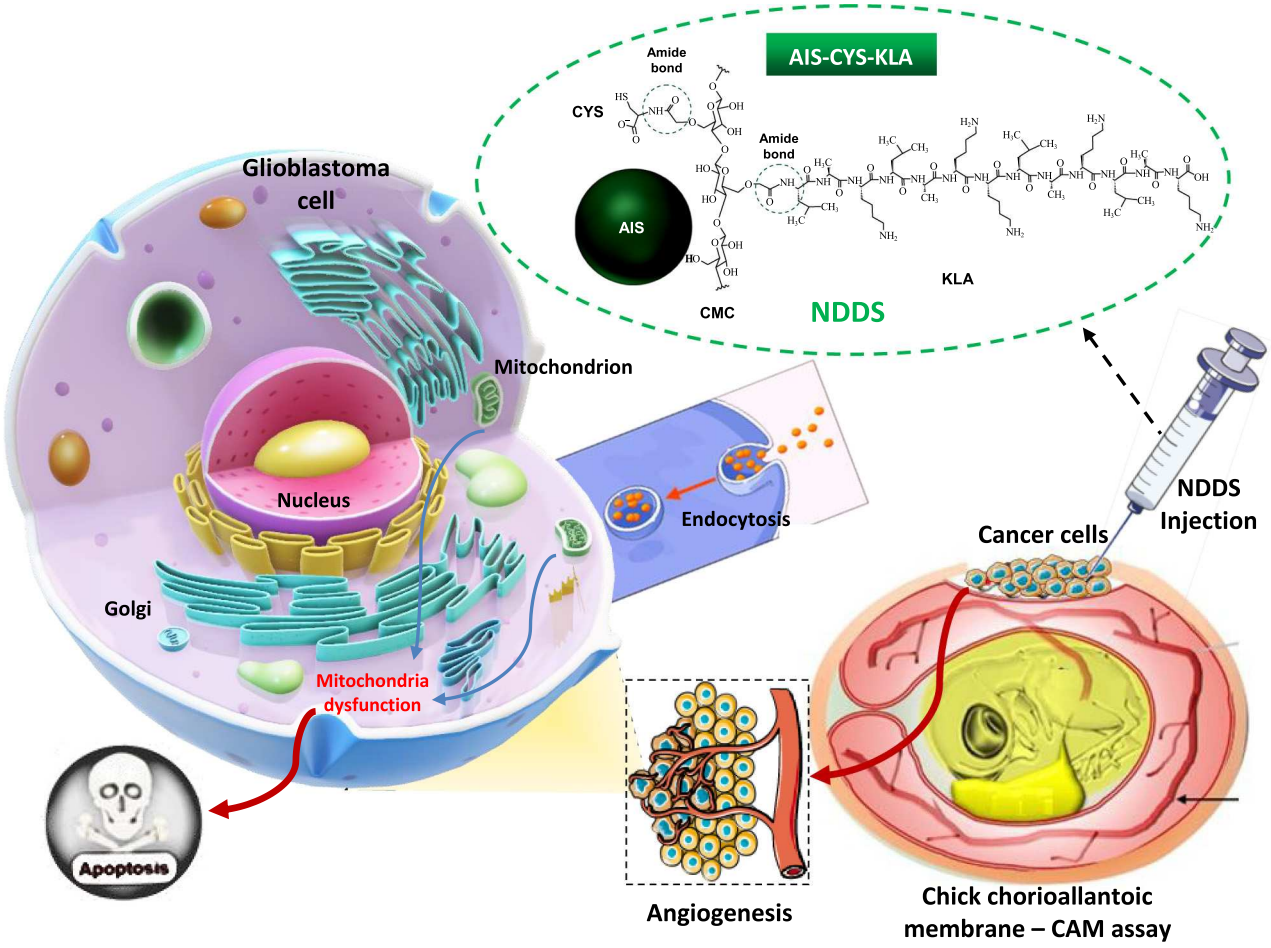

Fig. 10. Schematic illustration of the *in vitro* and *in vivo* CAM bioassays of photoluminescent biofunctionalized nanoarchitectonics for mitochondrial-targeted brain cancer bioimaging and therapy.

vessels, similar to that observed for DOX samples. More importantly, the area of the malignant tumor was significantly reduced by ~41% in the AIS-CYS-KLA nanohybrids compared to the control group (no reduction), and a more considerable decrease than the DOX-treated group (~35%). This is a crucial result when considering the toxic side-effects provoked by DOX used in cancer treatments. Thus, these novel nanotheranostic systems are anticipated to be suitable for simultaneously imaging and mitochondria-targeted therapy against brain cancer while protecting normal tissues and minimizing the highly potential systemic toxicity and collateral effects of conventional anticancer drug-based chemotherapy.

CRediT authorship contribution statement

Alexandra A. P. Mansur: Conceptualization, Methodology, Visualization, Investigation, Formal analysis, Writing - original draft, Writing - review & editing.

Mayara R. B. Paiva: Conceptualization, Methodology, Visualization, Investigation, Formal analysis, Writing - original draft, Writing - review & editing.

Oliver L. Cotta: Methodology, Visualization, Investigation, Formal analysis, Writing - original draft.

Luciana M. Silva: Methodology, Visualization, Investigation, Formal analysis, Writing - original draft.

Isadora C. Carvalho: Methodology, Visualization, Investigation, Formal analysis, Writing - original draft.

Nádia S. V. Capanema: Methodology, Visualization, Investigation, Formal analysis, Writing - original draft.

Sandhra M. de Carvalho: Methodology, Visualization, Investigation, Formal analysis, Writing - original draft.

Érica A. Costa: Methodology, Visualization, Investigation, Formal analysis, Writing - original draft.

Nelson R. Martin: Methodology, Visualization, Investigation, Formal analysis, Writing - original draft.

Roselene Ecco: Methodology, Visualization, Investigation, Formal analysis, Writing - review & editing.

Beatriz S. Santos: Methodology, Visualization, Investigation, Formal analysis, Writing - review & editing.

Silvia L. Fialho: Supervision, Conceptualization, Methodology, Visualization, Validation, Funding acquisition, Writing - original draft, Writing - review & editing, Resources, Project administration.

Zélia I. P. Lobato: Supervision, Conceptualization, Methodology, Visualization, Validation, Funding acquisition, Writing - original draft, Writing - review & editing, Resources, Project administration.

Herman S. Mansur: Supervision, Conceptualization, Methodology, Visualization, Validation, Funding acquisition, Writing - original draft, Writing - review & editing, Resources, Project administration.

Funding sources

This work was financially funded by the Brazilian Government Research Agencies: CNPq (PQ1A-303893/2018-4; PDS-103138/2020-0; PIBIC-2017-18; UNIVERSAL-421312/2018-1); FAPEMIG (UNIVERSAL-APQ-00291-18; PROBIC-2018); CAPES (PROINFRA-2010–2014; PROEX-2010/2019-2020; PNPD-2014-2020); and FINEP (CTINFRA/PROINFRA 2008/2010/2011/2018; SOS/Equipamentos/2018 -

01.19.0032.00).

Declaration of competing interest

The authors confirm no competing interests to declare regarding the publication of this article.

Acknowledgments

The authors would like to express thanks to the staff of the Center of Nanoscience, Nanotechnology, and Innovation-CeNano^{2}I/CEMUCASI/UFMG for spectroscopy and AFM analyses. Also, they express their gratitude to the staff at the Microscopy Center/UFMG for performing the HR-TEM analysis and Prof. Gustavo Batista de Menezes (ICB/UFMG) for the CLSM analysis.

We dedicate this research to all patients, doctors, and health professionals that tirelessly fight this everyday battle against cancer with diligence and courage.

Appendix A. Supplementary data

Supplementary data to this article can be found online at https://doi.org/10.1016/j.ijbiomac.2022.04.207.

References

[1] I.C. Carvalho, A.A.P. Mansur, S.M. Carvalho, H.S. Mansur, Nanotheranostics through mitochondria-targeted delivery with fluorescent peptidomimetic nanohybrids for apoptosis induction of brain cancer cells, Nanotheranostics 5 (2021) 213–239, https://doi.org/10.7150/ntno.54491.

[2] K. Du, Q. Xia, J. Sun, F. Feng, Visible light and glutathione dually responsive delivery of a polymer-conjugated temozolomide intermediate for glioblastoma chemotherapy, ACS Appl. Mater. Interfaces 13 (2021) 55851–55861, https://doi.org/10.1021/acsami.1c16962.

[3] M.T. Manzari, Y. Shamay, H. Kiguchi, N. Rosen, M. Scaltriti, D.A. Heller, Targeted drug delivery strategies for precision medicines, Nat. Rev. Mater. 6 (2021) 351–370, https://doi.org/10.1038/s41578-020-00269-6.

[4] K.W. Witwer, J. Wolfram, Extracellular vesicles versus synthetic nanoparticles for drug delivery, Nat. Rev. Mater. 6 (2021) 103–106, https://doi.org/10.1038/s41578-020-00277-6.

[5] P.S. Steeg, The blood-tumour barrier in cancer biology and therapy, Nat. Rev. Clin. Oncol. 18 (2021) 696–714, https://doi.org/10.1038/s41571-021-00529-6.

[6] T. Daubon, C. Léon, K. Clarke, L. Andrique, L. Salabert, E. Darbo, R. Pineau, S. Guérit, M. Maitre, S. Dedieu, et al., Deciphering the complex role of thrombospondin-1 in glioblastoma development, Nat. Commun. 10 (2019) 1146, https://doi.org/10.1038/s41467-019-08480-y.

[7] I. de Lázaro, D.J. Mooney, Obstacles and opportunities in a forward vision for cancer nanomedicine, Nat. Mater. 20 (2021) 1469–1479, https://doi.org/10.1038/s41563-021-01047-7.

[8] M.J. Mitchell, M.M. Billingsley, R.M. Haley, M.E. Wechsler, N.A. Peppas, R. Langer, Engineering precision nanoparticles for drug delivery, Nat. Rev. Drug Discov. 20 (2021) 101–124, https://doi.org/10.1038/s41573-020-0090-8.

[9] S. Sindhwani, A.M. Syed, J. Ngai, B.R. Kingston, L. Maiorino, J. Rothschild, P. MacMillan, Y. Zhang, N.U. Rajesh, T. Hoang, et al., The entry of nanoparticles into solid tumours, Nat. Mater. 19 (2020) 566–575, https://doi.org/10.1038/s41563-019-0566-2.

[10] A.A.P. Mansur, S.M. Carvalho, Z.I.P. Lobato, M.F. Leite, A.S. Cunha, H.S. Mansur, Design and development of polysaccharide-doxorubicin-peptide bioconjugates for dual synergistic effects of integrin-targeted and cell-penetrating peptides for cancer chemotherapy, Bioconjug. Chem. 29 (2018) 1973–2000, https://doi.org/10.1021/acs.bioconjchem.8b00208.

[11] G. Kandasamy, D. Maity, Multifunctional theranostic nanoparticles for biomedical cancer treatments - a comprehensive review, Mater. Sci. Eng., C 127 (2021), 112199, https://doi.org/10.1016/j.msec.2021.112199.

[12] A.J. Caires, H.S. Mansur, A.A.P. Mansur, I.C. Carvalho, S.C. Carvalho, A carboxymethylcellulose-mediated aqueous colloidal process for building plasmonic–excitonic supramolecular nanoarchitectures based on gold nanoparticles/ZnS quantum emitters for cancer theranostics, Green Chem. 23 (2021) 8260–8279, https://doi.org/10.1039/D1GC02508B.

[13] A.A.P. Mansur, J.C. Amaral-Júnior, S.M. Carvalho, I.C. Carvalho, H.S. Mansur, Cu-in-S/ZnS@carboxymethylcellulose supramolecular structures: fluorescent nanoarchitectures for targeted-theranostics of cancer cells, Carbohydr. Polym. 247 (2020), 116703, https://doi.org/10.1016/j.carbpol.2020.116703.

[14] I.C. Carvalho, H.S. Mansur, A.A.P. Mansur, S.M. Carvalho, L.C.A. de Oliveira, M. F. Leite, Luminescent switch of polysaccharide-peptide-quantum dot nanostructures for targeted-intracellular imaging of glioblastoma cells, J. Mol. Liq. 304 (2020), 112759, https://doi.org/10.1016/j.molliq.2020.112759.

[15] S.M. Carvalho, A.G. Leonel, A.A.P. Mansur, I.C. Carvalho, K. Krambrock, H. S. Mansur, Bifunctional magnetopolymersomes of iron oxide nanoparticles and carboxymethylcellulose conjugated with doxorubicin for hyperthermo-chemotherapy of brain cancer cells, Biomater. Sci. 7 (2019) 2102–2122, https://doi.org/10.1039/c8bm01528g.

[16] N. Zhao, L. Yan, X. Zhao, X. Chen, A. Li, D. Zheng, X. Zhou, X. Dai, F.-J. Xu, Versatile types of Organic/Inorganic nanohybrids: from strategic design to biomedical applications, Chem. Rev. 119 (2019) 1666–1762, https://doi.org/10.1021/acs.chemrev.8b00401.

[17] P. Gao, W. Pan, N. Li, B. Tang, Boosting cancer therapy with organelle-targeted nanomaterials, ACS Appl. Mater. Interfaces 11 (2019) 26529–26558, https://doi.org/10.1021/acsami.9b01370.

[18] H.S. Mansur, Quantum dots and nanocomposites, Wiley Interdiscip. Rev. Nanomed. Nanobiotechnol. 2 (2010) 113–129, https://doi.org/10.1002/wnan.78.

[19] A.A.P. Mansur, H.S. Mansur, A. Soriano-Araújo, Z.I.P. Lobato, Fluorescent nanohybrids based on quantum dot-chitosan-antibody as potential cancer biomarkers, ACS Appl. Mater. Interfaces 6 (2014) 11403–11412, https://doi.org/10.1021/am5019989.

[20] H.S. Mansur, A.A.P. Mansur, A. Soriano-Araújo, Z.I.P. Lobato, Beyond biocompatibility: an approach for the synthesis of ZnS quantum dot-chitosan nano-immunoconjugates for cancer diagnosis, Green Chem. 17 (2015) 1820–1830, https://doi.org/10.1039/C4GC02072C.

[21] G. Xu, S. Zeng, B. Zhang, M.T. Swihart, K.-T. Yong, P.N. Prasad, New generation cadmium-free quantum dots for biophotonics and nanomedicine, Chem. Rev. 116 (2016) 12234–12327, https://doi.org/10.1021/acs.chemrev.6b00290.

[22] R. Bilan, F. Fleury, I. Nabiev, A. Sukhanova, Quantum dot surface chemistry and functionalization for cell targeting and imaging, Bioconjug. Chem. 26 (2015) 609–624, https://doi.org/10.1021/acs.bioconjchem.5b00069.

[23] A. Shetty, S. Chandra, Inorganic hybrid nanoparticles in cancer theranostics: understanding their combinations for better clinical translation, Mater. Today Chem. 18 (2020), 100381, https://doi.org/10.1016/j.mtchem.2020.100381.

[24] A.A.P. Mansur, A.J. Caires, S.M. Carvalho, N.S.V. Capanema, I.C. Carvalho, H. S. Mansur, Dual-functional supramolecular nanohybrids of quantum dot/biopolymer/chemotherapeutic drug for bioimaging and killing brain cancer cells in vitro, Colloids Surf., B 184 (2019), 110507, https://doi.org/10.1016/j.colsurfb.2019.110507.

[25] J. Shi, Y. Jiang, X. Wang, H. Wu, D. Yang, F. Pan, Y. Su, Z. Jiang, Design and synthesis of organic–inorganic hybrid capsules for biotechnological applications, Chem. Soc. Rev. 43 (2014) 5192–5210, https://doi.org/10.1039/c4cs00108g.

[26] J. Zhou, L. Rao, G. Yu, T.R. Cook, X. Chen, F. Huang, Supramolecular cancer nanotheranostics, Chem. Soc. Rev. 50 (2021) 2839–2891, https://doi.org/10.1039/D0CS00011F.

[27] L. Su, Y. Feng, K. Wei, X. Xu, R. Liu, G. Chen, Carbohydrate-based macromolecular biomaterials, Chem. Rev. 121 (2021) 10950–11029, https://doi.org/10.1021/acs.chemrev.0c01338.

[28] I.C. Carvalho, H.S. Mansur, A.G. Leonel, A.A.P. Mansur, Z.I.P. Lobato, Soft matter polysaccharide-based hydrogels as versatile bioengineered platforms for brain tissue repair and regeneration, Int. J. Biol. Macromol. 182 (2021) 1091–1111, https://doi.org/10.1016/j.ijbiomac.2021.04.116.

[29] M.B. Noremylia, M.Z. Hassan, Z. Ismail, Recent advancement in isolation, processing, characterization and applications of emerging nanocellulose: a review, Int. J. Biol. Macromol. 206 (2022) 954–976, https://doi.org/10.1016/j.ijbiomac.2022.03.064.

[30] J. Wang, Y. Li, G. Nie, Multifunctional biomolecule nanostructures for cancer therapy, Nat. Rev. Mater. 6 (2021) 766–783, https://doi.org/10.1038/s41578-021-00315-x.

[31] X. Liu, F. Wu, Y. Ji, L. Yin, Recent advances in anti-cancer Protein/Peptide delivery, Bioconjug. Chem. 30 (2019) 305–324, https://doi.org/10.1021/acs.bioconjchem.8b00750.

[32] S. Mani, G. Swargiary, S. Tyagi, M. Singh, N.K. Jha, K.K. Singh, Nanotherapeutic approaches to target mitochondria in cancer, Life Sci. 281 (2021), 119773, https://doi.org/10.1016/j.lfs.2021.119773.

[33] S.E. Weinberg, N.S. Chandel, Targeting mitochondria metabolism for cancer therapy, Nat. Chem. Biol. 11 (2015) 9–15, https://doi.org/10.1038/nchembio.1712.

[34] S. Kim, H.Y. Nam, J. Lee, J. Seo, Mitochondrion-targeting peptides and peptidomimetics: recent progress and design principles, Biochemistry 59 (2020) 270–284, https://doi.org/10.1021/acs.biochem.9b00857.

[35] L. Jiang, L. Li, X. He, Q. Yi, B. He, J. Cao, W. Pan, Z. Gu, Overcoming drug-resistant lung cancer by paclitaxel loaded dual-functional liposomes with mitochondria targeting and pH-response, Biomaterials 52 (2015) 126–139, https://doi.org/10.1016/j.biomaterials.2015.02.004.

[36] H. He, L. Liu, E.E. Morin, M. Liu, A. Schwendeman, Survey of clinical translation of cancer nanomedicines - lessons learned from successes and failures, Acc. Chem. Res. 52 (2019) 2445–2461, https://doi.org/10.1021/acs.accounts.9b00228.

[37] W. Poon, B.R. Kingston, B. Ouyang, W. Ngo, W.C.W. Chan, A framework for designing delivery systems, Nat. Nanotechnol. 15 (2020) 819–829, https://doi.org/10.1038/s41565-020-0759-5.

[38] B. Ouyang, W. Poon, Y.-N. Zhang, Z.P. Lin, B.R. Kingston, A.J. Tavares, Y. Zhang, J. Chen, M.S. Valic, A.M. Syed, et al., The dose threshold for nanoparticle tumour delivery, Nat. Mater. 19 (2020) 1362–1371, https://doi.org/10.1038/s41563-020-0755-z.

[39] C.D. Arvanitis, G.B. Ferraro, R.K. Jain, The blood–brain barrier and blood–tumour barrier in brain tumours and metastases, Nat. Rev. Cancer 20 (2020) 26–41, https://doi.org/10.1038/s41568-019-0205-x.

[40] K. Aldape, K.M. Brindle, L. Chesler, R. Chopra, A. Gajjar, M.R. Gilbert, N. Gottardo, D.H. Gutmann, D. Hargrave, E.C. Holland, et al., Challenges to curing primary brain tumours, Nat. Rev. Clin. Oncol. 16 (2019) 509–520, https://doi.org/10.1038/s41571-019-0177-5.
[41] A.I. Khan, X. Cai, Y. Song, Z. Lyu, D. Du, P. Dutta, Y. Lin, Overcoming blood–brain barrier transport: advances in nanoparticle-based drug delivery strategies, Mater. Today 10 (2020) 112–125, https://doi.org/10.1016/j.mattod.2020.02.001.
[42] S. Wilhelm, A.J. Tavares, Q. Dai, S. Ohta, J. Audet, H.F. Dvorak, W.C.W. Chan, Analysis of nanoparticle delivery to tumors, Nat. Rev. Mater. 1 (2016) 16014, https://doi.org/10.1038/natrevmats.2016.14.
[43] R. Swadi, G. Mather, B.L. Pizer, P.D. Losty, V. See, D. Moss, Optimising the chick chorioallantoic membrane xenograft model of neuroblastoma for drug delivery, BMC Cancer 18 (2018) 28, https://doi.org/10.1186/s12885-017-3978-x.
[44] A.K. Mapanao, P.P. Che, P. Sarogni, P. Sminia, E. Giovannetti, V. Voliani, Tumor grafted – chick chorioallantoic membrane as an alternative model for biological cancer research and conventional/nanomaterial-based theranostics evaluation, Expert Opin. Drug Metab. Toxicol. 17 (2021) 947–968, https://doi.org/10.1080/17425255.2021.1879047.
[45] N. Mangir, S. Dikici, F. Claeyssens, S. MacNeil, Using ex ovo Chick chorioallantoic membrane (CAM) assay to evaluate the biocompatibility and angiogenic response to biomaterials, ACS Biomater. Sci. Eng. 5 (2019) 3190–3200, https://doi.org/10.1021/acsbiomaterials.9b00172.
[46] Z. Zuo, T. Syrovets, Y. Wu, S. Hafner, I. Vernikouskaya, W. Liu, G. Ma, T. Weil, T. Simmet, V. Rasche, The CAM cancer xenograft as a model for initial evaluation of MR labelled compounds, Sci. Rep. 7 (2017) 46690, https://doi.org/10.1038/srep46690.
[47] A. Raevskaya, V. Lesnyak, D. Haubold, V. Dzhagan, O. Stroyuk, N. Gaponik, D.R. T. Zahn, A. Eychmüller, A fine size selection of brightly luminescent water-soluble Ag–In–S and Ag–In–S/ZnS quantum dots, J. Phys. Chem. C 121 (2017) 9032–9042, https://doi.org/10.1021/acs.jpcc.7b00849.
[48] M.L.A. Aguilera, M. Ortega-López, V.M.S. Resendiz, J.A. Hernández, M.A. G. Trujillo, Some physical properties of chalcopyrite and orthorhombic AgInS2 thin films prepared by spray pyrolysis, Mater. Sci. Eng., B 102 (2003) 380–384, https://doi.org/10.1016/S0921-5107(02)00626-8.
[49] S. Prasad, I. Mandal, S. Singh, A. Paul, B. Mandal, R. Venkatramani, R. Swaminathan, Near UV-visible electronic absorption originating from charged amino acids in a monomeric protein, Chem. Sci. 8 (2017) 5416–5433, https://doi.org/10.1039/C7SC00880E.
[50] M. Zabadaj, P. Ciosek-Skibinska, Quantum dots—assisted 2D fluorescence for pattern based sensing of amino acids, oligopeptides and neurotransmitters, Sensors 19 (2019) 3655, https://doi.org/10.3390/s19173655.
[51] I.A. Mir, V.S. Radhakrishanan, K. Rawat, T. Prasad, H.B. Bohidar, Bandgap tunable AgInS based quantum dots for high contrast cell imaging with enhanced photodynamic and antifungal applications, Sci. Rep. 8 (2018) 9322, https://doi.org/10.1038/s41598-018-27246-y.
[52] L.B. Kiss, J. Soderlund, G.A. Niklasson, C.G. Granqvist, New approach to the origin of lognormal size distributions of nanoparticles, Nanotechnology 10 (1999) 25–28, https://doi.org/10.1088/0957-4484/10/1/006.
[53] T. Torimoto, M. Tada, M. Dai, T. Kameyama, S. Suzuki, S. Kuwabata, Tunable photoelectrochemical properties of chalcopyrite AgInS2 nanoparticles size-controlled with a photoetching technique, J. Phys. Chem. 116 (2012) 21895–21902, https://doi.org/10.1021/jp307305q.
[54] Y. Hamanaka, T. Ogawa, M. Tsuzuki, Photoluminescence properties and its origin of AgInS2 quantum dots with chalcopyrite structure, J. Phys. Chem. C 115 (2011) 1786–1792, https://doi.org/10.1021/jp110409q.
[55] A. Barth, The infrared absorption of amino acid side chains, Prog. Biophys. Mol. Biol. 74 (2001) 141–173, https://doi.org/10.1016/s0079-6107(00)00021-3.
[56] U. Resch-Genger, M. Grabolle, S. Cavaliere-Jaricot, R. Nitschke, T. Nann, Quantum dots versus organic dyes as fluorescent labels, Nat. Methods 5 (2008) 763–775, https://doi.org/10.1038/nmeth.1248.
[57] R.E. Bailey, A.M. Smith, S. Nie, Quantum dots in biology and medicine, Physica E 25 (2004) 1–12, https://doi.org/10.1016/j.physe.2004.07.013.
[58] A.A.P. Mansur, H.S. Mansur, S.M. Carvalho, A.J. Caires, One-pot aqueous synthesis of fluorescent Ag-In-Zn-S quantum dot/polymer bioconjugates for multiplex optical bioimaging of glioblastoma cells, Contrast Media Mol. Imaging 2017 (2017), 3896107, https://doi.org/10.1155/2017/3896107.
[59] T. Li, W. Gao, J. Liang, M. Zha, Y. Chen, Y. Zhao, C. Wu, Biscysteine-bearing peptide probes to reveal extracellular thiol-disulfide exchange reactions promoting cellular uptake, Anal. Chem. 89 (2017) 8501–8508, https://doi.org/10.1021/acs.analchem.7b02084.
[60] Y. Wei, T. Tang, H.B. Pang, Cellular internalization of by stander nanomaterial induced by TAT-nanoparticles and regulated by extracellular cysteine, Nat. Commun. 40 (2019) 3646, https://doi.org/10.1038/s41467-019-11631-w.
[61] R. Zhang, X. Qin, F. Kong, P. Chen, G. Pan, Improving cellular uptake of therapeutic entities through interaction with components of cell membrane, Drug Deliv. 26 (2019) 328–342, https://doi.org/10.1080/10717544.2019.1582730.
[62] B.K. Ahir, H.H. Engelhard, S.S. Lakka, Tumor development and angiogenesis in adult brain tumor: glioblastoma, Mol. Neurobiol. 57 (2020) 2461–2478, https://doi.org/10.1007/s12035-020-01892-8.
[63] W. Wick, T. Gorlia, M. Bendszus, M. Taphoorn, F. Sahm, I. Harting, A.A. Brandes, W. Taal, J. Domont, A. Idbaih, et al., Lomustine and bevacizumab in progressive glioblastoma, N. Engl. J. Med. 377 (2017) 1954–1963, https://doi.org/10.1056/NEJMoa1707358.
[64] M. Nishikawa, A. Inoue, T. Ohnishi, H. Yano, Y. Kanemura, S. Kohno, S. Ohue, S. Ozaki, S. Matsumoto, S. Suehiro, et al., CD44 expression in the tumor periphery predicts the responsiveness to bevacizumab in the treatment of recurrent glioblastoma, Cancer Med. 10 (2021) 2013–2025, https://doi.org/10.1002/cam4.3767.
[65] D. Ribatti, T. Annese, R. Tamma, The use of the chick embryo CAM assay in the study of angiogenic activity of biomaterials, Microvasc. Res. 131 (2020), 104026, https://doi.org/10.1016/j.mvr.2020.104026.
[66] I. Valiulytė, R. Curkūnavičiūtė, L. Ribokaitė, A. Kazlauskas, M. Vaitkevičiūtė, K. Skauminas, A. Valančiūtė, The anti-tumorigenic activity of Sema3C in the chick embryo chorioallantoic membrane model, Int. J. Mol. Sci. 20 (2019) 5672, https://doi.org/10.3390/ijms20225672.
[67] W. Li, M. Yalcin, D.J. Bharali, Q. Lin, K. Godugu, K. Fujioka, K.A. Keating, S. A. Mousa, Pharmacokinetics, biodistribution, and anti-angiogenesis efficacy of diamino propane tetraiodothyroacetic acid-conjugated biodegradable polymeric nanoparticle, Sci. Rep. 9 (2019) 9006, https://doi.org/10.1038/s41598-019-44979-6.
[68] F.G. Lopes, K.A. Oliveira, R.G. Lopes, G.G. Poluceno, C. Simioni, G.S. Pescador, C. M. Bauer, M. Maraschin, R.B. Derner, R.C. Garcez, et al., Anti-cancer effects of fucoxanthin on human glioblastoma cell line, Anticancer Res. 40 (2020) 6799–6815, https://doi.org/10.21873/anticanres.14703.
[69] A. Uvez, S. Aydinlik, O.B.B. Esener, M. Erkisa, D. Karakus, E.I. Armutak, Synergistic interactions between resveratrol and doxorubicin inhibit angiogenesis both in vitro and in vivo, Pol. J. Vet. Sci. 23 (2020) 571–580, https://doi.org/10.24425/pjvs.2020.135803.
[70] M.R.B. Paiva, G.F. Andrade, L.F.N. Dourado, B.F.M. Castro, S.L. Fialho, E.M. B. Sousa, A. Silva-Cunha, Surface functionalized mesoporous silica nanoparticles for intravitreal application of tacrolimus, J. Biomater. Appl. 35 (2021) 1019–1033, https://doi.org/10.1177/0885328220977605.
[71] F. Durupt, D. Koppers-Lalic, B. Balme, L. Budel, O. Terrier, B. Lina, L. Thomas, R. C. Hoeben, M. Rosa-Calatrava, The chicken chorioallantoic membrane tumor assay as model for qualitative testing of oncolytic adenoviruses, Cancer Gene Ther. 19 (2012) 58–68, https://doi.org/10.1038/cgt.2011.68.
[72] D. Ribatti, The chick embryo chorioallantoic membrane (CAM). A multifaceted experimental model, Mech. Dev. 141 (2016) 70–77, https://doi.org/10.1016/j.mod.2016.05.003.
[73] A. Rojiani, M. Amyn, K. Dorovini-Zis, Glomeruloid vascular structures in glioblastoma multiforme: an immunohistochemical and ultrastructural study, J. Neurosurg. 85 (1996) 1078–1084, https://doi.org/10.3171/jns.1996.85.6.1078.
[74] B.O.P. Gonçalves, S.L. Fialho, B.R. Silvestrini, I.F.G. Sena, G.S.P. dos Santos, D. A. Gomes, L.M. Silva, Central nervous system (CNS) tumor cell heterogeneity contributes to differential platinum-based response in an in vitro 2D and 3D cell culture approach, Exp. Mol. Path. 116 (2020), 104520, https://doi.org/10.1016/j.yexmp.2020.104520.
[75] E. Preis, J. Schulze, B. Gutberlet, S.R. Pinnapireddy, J. Jedelská, U. Bakowsky, The chorioallantoic membrane as a bio-barrier model for the evaluation of nanoscale drug delivery systems for tumour therapy, Adv. Drug Deliv. Rev. 174 (2021) 317–336, https://doi.org/10.1016/j.addr.2021.04.022.
[76] T. Strojnik, R. Kavalar, T.A. Barone, R.J. Plunkett, Experimental model and immunohistochemical comparison of U87 human glioblastoma cell xenografts on the chicken chorioallantoic membrane and in rat brains, Anticancer Res. 30 (2010) 4851–4860.
[77] M. Izci, C. Maksoudian, B.B. Manshian, S.J. Soenen, The use of alternative strategies for enhanced nanoparticle delivery to solid tumors, Chem. Rev. 121 (2021) 1746–1803, https://doi.org/10.1021/acs.chemrev.0c00779.
[78] J. Kapitulnik, C. Benaim, S. Sasson, Endothelial cells derived from the blood-brain barrier and islets of langerhans differ in their response to the effects of bilirubin on oxidative stress under hyperglycemic conditions, Front. Pharmacol. 3 (2012) 131, https://doi.org/10.3389/fphar.2012.00131.
[79] L. Kozlovskaya, M. Abou-Kaoud, D. Stepensky, Quantitative analysis of drug delivery to the brain via nasal route, J. Control. Release 189 (2014) 133–140, https://doi.org/10.1016/j.jconrel.2014.06.053.
[80] R.A. Yokel, Direct nose to the brain nanomedicine delivery presents a formidable challenge, Wiley Interdiscip. Rev. Nanomed. Nanobiotechnol. 14 (2022), e1767, https://doi.org/10.1002/wnan.1767.